Seasonal dependence of northern high latitude upper thermospheric winds: A quiet-time climatological study based on ground-based and space-based measurements

Manbharat Dhadly[1], John Emmert[2], Douglas Drob[2], Mark Conde[3], Eelco Doornbos[4], Gordon Shepherd[5], Jonathan Makela[6], Qian Wu[7], Rick Niciejewski[8], and Aaron Ridley[8]

[1]National Research Council Postdoctoral Research Associate, Space Science Division, Naval Research Laboratory, Washington DC, USA
[2]Space Science Division, Naval Research Laboratory, Washington DC, USA
[3]Geophysical Institute, University of Alaska Fairbanks, Alaska, USA
[4]Aerospace Engineering, Delft University of Technology, The Netherlands
[5]Centre for Research in Earth and Space Science, York University, Canada
[6]Electrical and Computer Engineering, University of Illinois, Illinois, USA
[7]High Altitude Observatory, UCAR, Colorado, USA
[8]Climate and Space Sciences and Engineering, University of Michigan, Ann Arbor, Michigan, USA

Key Points:

- First ever investigation of the large scale seasonal dependence of northern high latitude upper thermospheric winds in magnetic coordinates.
- Results show progressive intensification of wind circulation from winter to equinox to summer.
- The vorticity increases from winter to summer. In all the seasons, the strongest divergences occur primarily in and above auroral latitudes.

This is the author manuscript accepted for publication and has undergone full peer review but has not been through the copyediting, typesetting, pagination and proofreading process, which may lead to differences between this version and the Version of Record. Please cite this article as doi: 10.1002/2016JA023688

Corresponding author: Manbharat Dhadly, manbharat.dhadly.ctr.in@nrl.navy.mil

Abstract

This paper investigates the large scale seasonal dependence of geomagnetically quiet-time, northern high latitude F-region thermospheric winds by combining extensive observations from eight ground-based (optical remote sensing) and three space-based (optical remote sensing and in situ) instruments. To provide a comprehensive picture of the wind morphology, data is assimilated into a seasonal empirical vector wind model as a function of season, latitude, and local time in magnetic coordinates. The model accurately represents the behavior of the constituent datasets. There is good general agreement among the various datasets, but there are some major offsets between GOCE and the other datasets, especially on the duskside. The assimilated wind patterns exhibit a strong and large duskside anticyclonic circulation cell, sharp latitudinal gradients in the duskside auroral zone, strong antisunward winds in the polar cap, and a weaker tendency toward a dawnside cyclonic circulation cell. The high latitude wind system shows a progressive intensification of wind patterns from winter to equinox to summer. The latitudinal extent of the duskside circulation cell does not depend strongly on season. Zonal winds show a mainly diurnal variation (2 extrema) around polar and middle latitudes, and semidiurnal variation (4 extrema) at auroral latitudes; meridional winds are primarily diurnal at all high latitudes. The strength of zonal winds channeling through the auroral zone on the duskside is strongest in the summer season. The vorticity of the wind pattern increases from winter to summer, whereas divergence is maximum in equinox. In all three seasons, divergence is weaker than vorticity.

1 Introduction

Thermospheric neutral wind circulation at high latitudes is a key component of global space weather research, primarily because neutral winds are strongly coupled to the ionospheric convecting plasma via momentum exchange between ions and neutrals [e.g., *Meriwether et al.*, 1973; *Roble et al.*, 1982; *Mikkelsen and Larsen*, 1983; *Killeen and Roble*, 1988; *Thayer and Killeen*, 1993; *Richmond et al.*, 2003; *Kwak and Richmond*, 2007]. Neutral winds at high latitudes are predominantly controlled by heating-induced pressure gradients (caused by absorption of solar ultraviolet irradiance, Joule heating, particle precipitation, and other heating sources), momentum transfer between ion and neutrals, inertial forces (Coriolis and centrifugal), tidal forcing from below, and internal small-scale instabilities. The time varying interplay among these drivers results in the formation of a highly complex thermospheric wind circulation with a prominent anticyclonic cell on the duskside of the magnetic pole, strong antisunward winds over the pole, and a weaker cyclonic tendency on the dawnside. Given the controlling factors, previous systematic studies have shown that the high latitude neutral wind circulation responds strongly to changes in season, solar activity, interplanetary magnetic field (IMF), and geomagnetic activity [e.g., *Hernandez and Roble*, 1976; *Babcock and Evans*, 1979; *McCormac and Smith*, 1984; *McCormac et al.*, 1985, 1987; *Killeen*, 1987; *Rees and Fuller-Rowell*, 1989; *Sica et al.*, 1989; *Aruliah et al.*, 1991a,b; *Mccormac et al.*, 1991; *Aruliah et al.*, 1996; *Niciejewski et al.*, 1992; *Killeen et al.*, 1995; *Fuller-Rowell et al.*, 1996; *Emmert et al.*, 2006a, 2008; *Förster et al.*, 2008; *Wu et al.*, 2008; *Witasse et al.*, 1998]. As a consequence of the high latitude energy and momentum inputs, the thermosphere's most dynamic weather exists at high latitudes and variability is always present in thermospheric winds even during quiet geomagnetic conditions (herein called "quiet-time").

High latitude thermospheric winds have been intensively studied over the past several decades, but their large scale response to the change in seasons is still not well understood. This is due in part to historically sparse neutral wind observations, especially at high latitudes: Most previous seasonal studies based on observational data are focused on either nighttime climatology or data from individual instruments with limited spatial coverage [e.g., *Hernandez and Roble*, 1976; *Babcock and Evans*, 1979; *Aruliah et al.*, 1991a, 1996; *Emmert et al.*, 2006b]. No single observational dataset provides comprehensive space-time coverage of the high latitude wind system. Over the past two decades, geospace empirical observational databases have grown significantly. For the first time, this permits statistical analysis of daytime as well as nighttime high latitude horizontal winds as a function of season, latitude, and local time. Utilizing extensive observations from ground and space-based instruments, this paper examines for the first time, the large scale seasonal response of quiet-time (defined by planetary K_p index < 3) northern high latitude (magnetic latitudes, or MLAT, above 45N) upper thermospheric neutral wind circulation under low to moderate solar extreme ultraviolet (EUV) irradiance conditions (defined by daily 10.7 cm solar radio flux ($F_{10.7}$) between 80 and 150).

To obtain a comprehensive seasonal understanding of the northern high latitude geospace neutral wind system, we amalgamated daytime and nighttime extensive measurements recorded by 11 ground-based (optical remote sensing) and space-based (optical remote sensing and in situ) instruments at various northern high latitudes. These instruments, their locations, data coverage, and citations are shown in Table 1. Out of these 11 instruments, six are ground-based narrow field Fabry-Perot interferometers (FPIs), two are ground-based wide field Scanning Doppler imaging Fabry-Perot interferometers (SDIs), and three are space-based instruments: The WIND Imaging Interferometer (WINDII) on the Upper Atmosphere Research Satellite (UARS), the Gravity Field and Steady-State Ocean Circulation Explorer (GOCE) accelerometer, and the Wind and Temperature Spectrometer (WATS) on Dynamic Explorer 2 (DE2). Construction of the empirical model provides an additional opportunity to inter-compare these data sets. These instruments operated independently of each other, and have different technical implementations, modes of operations, and data processing algorithms. As a result, these diverse datasets present different geometries, different spatial and solar coverage, and possible mutual biases. Fusion of these diverse data into an empirical climatology is thus a formidable challenge.

The present empirical Horizontal Wind Model (HWM) [*Drob et al.*, 2008, 2015] formulation based on the early works of *Hedin et al.* [1996] has some limitations at high latitudes. For example, it describes global wind patterns in geographic coordinates. Because ionospheric plasma motions are naturally organized by the geomagnetic field and ion drag is one of the primary drivers of neutral winds at high latitudes, this leads to better organization of high latitude neutral winds in magnetic coordinates than in geographic coordinates [*Hays et al.*, 1984; *Richmond*, 1995; *Emmert et al.*, 2008, 2010]. Therefore, in this study, we assimilate wind data in geomagnetic latitude and geomagnetic local time. To our knowledge, the study presented here, is the first attempt to combine multiple wind datasets to determine the quiet-time seasonal dependence of high latitude upper thermospheric wind patterns in geomagnetic coordinates. In past, *Richmond et al.* [2003] utilized magnetic coordinates to analyze the IMF dependence of neutral winds measured by the Wind Imaging Interferometer (WINDII) at southern high latitudes. *Förster et al.* [2008, 2011] studied the IMF dependence of thermospheric winds using CHAMP data in magnetic coordinates. Recently, *Xiong et al.* [2015] used magnetic coordinates to study the seasonal dependence of global disturbance zonal winds derived from CHAMP data.

To obtain a complete diagnosis of the climatological high latitude wind patterns, we examine the seasonal behavior of the associated large scale vorticity (vertical component) and divergence patterns of the horizontal wind components. To our knowledge, this study is also the first ever to address the seasonal dependence of high latitude thermospheric vorticity and divergence. Vorticity is the measure of shears or any curvature present in the horizontal wind flows. At high latitudes, vorticity is primarily driven by ion drag, and divergence is primarily associated with vertical motions induced by heating or cooling of thermospheric air [*Mayr and Harris*, 1978; *Volland*, 1979; *Hays et al.*, 1984; *Thayer and Killeen*, 1991, 1993; *Förster et al.*, 2011; *Kwak and Richmond*, 2014]. The strengths of vorticity and divergence induced by various momentum and energy sources are thus commonly used to gain insight into the strength of their key drivers. In vorticity field, vorticity is zero when either the wind field is uniform or shears reverse their direction, thus this transition region in vorticity field can be exploited to determine the spatial extent of neutral circulation. In addition, any systematic trend in divergence of the horizontal wind can highlight the high latitude regions where most of the heating/cooling is occurring in the thermosphere.

In this work, for a comprehensive seasonal comparison, we have divided high latitudes into three regions: the polar latitudes (80–90N MLAT), auroral latitudes (60–80N MLAT), and middle latitudes (45–60N MLAT). This study is organized as follows. Section 2 describes the measurements from various ground and space stations and applied data quality control. Section 3 describes the methodology implemented for data assimilation in magnetic coordinates. The results of the study are presented in section 4. Sections 4.1 and 4.2 discuss the validation and statistical performance of derived quiet-time climatological zonal and meridional wind fits against the observational data. Biases or discrepancies among the various datasets are also discussed in these sections. Section 5.1 highlights the seasonal variation in quiet-time zonal and meridional winds fields. The vorticity and divergence of the wind fields, and their seasonal dependences, are addressed in section 5.2. Finally, conclusions are presented in section 6.

2 Observational Data

The analysis considers long-term thermospheric F-region wind observations from three satellite instruments and eight ground-based optical spectrometers spanning the years 1981 to 2015 during geomagnetically quiet conditions (3-hour K_p index less than 3), northern magnetic latitudes above 45N (although global satellite data are included in our empirical model to stabilize the fits), and altitudes between 210 km and 320 km. Basic theoretical considerations indicate that altitudinal variations in this region will be strongly damped by the large effective viscosity [e.g., *Kohl and King*, 1967]. Observational studies by *Killeen et al.* [1982] and *Wharton et al.* [1984] using DE2 F-region neutral wind observations averaged over multiple orbits show small variation in horizontal winds with increasing altitude. Further, *Emmert et al.* [2002] found that, in a statistical sense, there is no significant altitude variation in F-region climatological disturbance winds derived from UARS WINDII profiles. Thus, this climatological study, while technically representing height-averaged winds, should provide an accurate representation of winds anywhere between 210 and 320 km altitude.

Because most of the measurements were made after the strong solar maxima of cycles 21 and 22, the data primarily represent low to moderate solar flux conditions [*Drob et al.*, 2008]. The solar flux dependence of the high latitude winds is not well understood, but to avoid the possibility of very high or very low solar flux conditions skewing our climatological results, we included only wind observations for which the daily 10.7 cm solar radio flux ($F_{10.7}$) was between 80 and 150 solar flux units (1 sfu = 10^{-22} W m^{-2} Hz^{-1}). Subsequent analysis of $F_{10.7}$ effects are left for future work. For analysis, we sorted the quiet-time data into three seasonal bins, with each bin covering four months of wind data: December solstice (Nov–Feb), equinox (Mar, Apr, Sep, Oct), and June solstice (May–Aug). The average $F_{10.7}$ for data in December solstice, equinox, and June solstice bins are $\sim$114 sfu, 115 sfu, and 106 sfu; the small differences among these averages indicate that any $F_{10.7}$ dependence in the winds will not significantly alias into the estimated seasonal dependence.

Table 1 and Figure 1 summarize the sampling characteristics and spatial coverage, in geomagnetic coordinates, of the data used in our analysis. A brief description is given below.

2.1 Ground-based Observations

In recent decades, the ground-based optical remote sensing of the thermosphere using Fabry-Perot spectrometers (FPSs) for winds and temperatures have become a popular tool; several variants of FPS are currently in use (e.g., narrow field FPIs and wide field SDIs). They derive winds from Doppler shifts in the nighttime naturally occurring red line optical emissions (630 nm wavelength), which are generated from the dissociative recombination of O_2^+. Typically, FPIs take measurements in 4 to 8 directions with a narrow field of view of $\sim$1 degree, which maps to a spatial extent of 4–5 km at station zenith when projected at an altitude of 240–250 km (assumed peak volume emission altitude). On the other hand, SDIs use all-sky fore-optics coupled to a separation scanned etalon to collect optical emission profiles simultaneously from many tens of locations (typically 115) across the sky; the typical full field of view is 140 degrees. Although both SDIs and FPIs use Doppler spectroscopy of naturally occurring optical emissions from the thermosphere, there are significant differences in their operation. A detailed comparison between these two measuring techniques is provided in *Dhadly et al.* [2015]. The major limitation of current ground-based FPIs and SDIs is that they operate only during nighttime. Thus, at high latitudes their local time coverage is much better in winter than summer.

We used data from the following FPIs; detailed descriptions of the instruments used in this study, including their observation mode and data reduction technique, may be found in in the cited references: Thule FPI (herein labeled TH FPI) [*Meriwether et al.*, 1988; *Killeen et al.*, 1995], Resolute Bay FPI (RB FPI) [*Wu et al.*, 2004, 2008], Søndre Strømfjord FPI (SS FPI) [*Meriwether et al.*, 1984; *Meriwether and Shih*, 1987; *Niciejewski et al.*, 1989; *Killeen et al.*, 1995], Millstone Hill FPI (MH FPI) [*Sipler et al.*, 1991; *Buonsanto et al.*, 1992; *Fejer et al.*, 2002; *Emmert et al.*, 2003], Peach Mountain FPI (PM FPI) [*Makela et al.*, 2011, 2012], and Urbana Atmospheric Observatory (UR FPI, also called the MiniME Doppler Imaging FPI) [*Makela et al.*, 2011, 2012]. For SDIs located at Poker Flat Research Range (PF SDI) and Toolik Lake Research Station (TL SDI), the details are presented in *Conde and Smith* [1995, 1998]; *Anderson et al.* [2012]; *Dhadly et al.* [2015]; *Dhadly and Conde* [2016]. Additional details for all instruments, observation modes, and wind estimation procedures used by the FPIs and SDIs are available from the CEDAR Madrigal database (http://cedar.openmadrigal.org/).

A cloud cover index (on scale 0–10, where 0 is clear and 10 is overcast) was regularly monitored by several FPI observatories; we excluded periods of substantial cloud cover (cloud cover index > 5) in our analysis. The Urbana and Peach Mountain FPIs used a different cloud cover monitoring system. These observatories use a sensor that returns the local cloud conditions in terms of a difference between the temperature of the sky and the ambient ground level temperature; any sensor temperature reading below $-20°$C indicates good viewing conditions. For these two observatories, we excluded any data when the cloud sensor temperature was above $-20°$C. The details of the cloud index for each FPI can be found in the description files on the CEDAR database. For SDIs, we eliminated periods of substantial cloud cover by assessing all-sky wind summary plots, all-sky temperature, and emission intensity data, as described by *Dhadly and Conde* [2016].

The SDI instruments located at Poker and Toolik measure upper thermospheric winds at high temporal and spatial resolution covering 60–74N MLAT. As a result, there is a dense swath of wind measurements at these latitudes. These SDIs are configured to start taking wind measurements when the Sun goes 8 degrees below horizon; therefore, there is always a possibility of twilight contaminating the Doppler spectra of the first few exposures in the beginning of an observation cycle. For both stations, to avoid any twilight contamination in this analysis, we excluded the first four exposures of each observation cycle.

All of the ground-based stations listed in Table 1 measure the thermospheric wind at multiple locations (latitude and longitude) within their field of view. The table lists the locations of the instruments, not the locations of their observations in the thermosphere. The observation locations in the thermosphere are dependent on the viewing geometry and the effective altitude of the emission layer. The peak volume emission altitude is typically assumed near 240–250 km, but it changes with solar zenith angle and solar cycle. FPI and SDI techniques of thermospheric wind measurements commonly assume that the 630 nm peak volume emission altitude is centered around 240-250 km and that there are no significant altitude variation in horizontal wind. However, at high latitudes, the 630 nm emission layer can peak lower in altitude in the presence of auroral precipitation, whereas it can peak much higher in the presence of soft or no auroral precipitation [*Sica et al.*, 1986]. So, the 630 nm emissions recorded by FPIs and SDIs comes from a broad range of F-region altitudes and in this climatology we are averaging over all those altitudes.

2.2 Space-based Observations

For a complete seasonal climatology of the high latitude winds, nighttime as well as daytime wind measurements are needed. For daytime coverage, we included in our analysis data from three space-based instruments: DE2 WATS, UARS WINDII, and GOCE. The magnetic latitude coverage of these data is given in Table 1 in Quasi-Dipole coordinates [*Richmond*, 1995; *Emmert et al.*, 2010].

Doornbos et al. [2013, 2014] derived in situ crosswinds (i.e., the horizontal wind component perpendicular to the direction of orbital motion with respect to the atmosphere) at 10 s cadence from GOCE accelerometer observations of satellite non-gravitational forces. These forces include aerodynamic drag and lift as well as radiation pressure. Due to the fact that the GOCE mission was not designed for aeronomy purposes, the maturity level of the crosswind data is perhaps lower than the other data types described here, and in any case the data is of a different nature. The processing, detailed in *Doornbos* [2011] is based on comparing the observed drag and lift accelerations with those from a satellite aerodynamic model, and determining the wind motion that reconciles the aerodynamic model with the observed acceleration.

The GOCE crosswind observations cover altitudes 220–280 km and years 2009–2013. The satellite was in a near-circular polar and sun-synchronous orbit with ascending equator crossings drifting between 1800 and 1936 local solar time over its lifetime. Because of its 96.7 degree inclination, GOCE's orbit reached maximum northern geographic latitudes of up to 83.3 degrees on the sunward side of the pole. It therefore produced a dataset with limited magnetic local time coverage (mostly in the dawn and dusk sectors), as shown in Figure 1.

UARS WINDII was a Michelson interferometer that observed airglow emissions at the Earth's limb [*Shepherd et al.*, 1993, 2012; *Emmert et al.*, 2004]; we used version 5.11 level 2 data in this study. Most of the daytime WINDII upper thermospheric wind data was obtained at 557.7 nm (green line) wavelength; relatively fewer WINDII nighttime observations were obtained at 630.0 nm (red line), as illustrated in Figure 1. The WINDII data consist of height profiles; we averaged each profile over the altitude range 210–320 km prior to analysis. Validation of the data is described by *Gault et al.* [1996].

WATS on DE2 was a spectrometer that measured in situ zonal neutral winds along the spacecraft track in the polar orbit [*Spencer et al.*, 1981, 1982; *Killeen and Roble*, 1988; *Killeen et al.*, 1988]. WATS wind measurements cover altitudes from 200 to 880 km. Because this study is focused on neutral wind dynamics at F-region altitudes, we selected data between 210 and 320 km. Most of the WATS measurements were taken during the solar maximum period and above 300 km altitude, so that a significant fraction of the WATS data was excluded by our solar flux and altitude selection criteria.

2.3 Spatio-temporal Coverage

Some of the instruments listed in Table 1 (the SDIs and GOCE) produced spatially and temporally dense datasets. Over multiple trails, we found that the SDI and GOCE data regions are so oversampled that they completely dominate the statistical wind fits over the other stations. To prevent those datasets from dominating our statistical wind model, we de-weighted them by taking a random subset of those datasets. For the Poker Flat and Toolik Lake SDIs, we settled on randomly selected only 2.5% of these data for the December solstice and equinox fits. During June solstice, Poker Flat provided the only ground-based observations at or above 60N magnetic latitude; for this season, we settled on selecting 10% of the data in the fit. As with the SDI data, we de-weighted spatially and temporally dense GOCE dataset by taking a random 3.3% subset in the December solstice and equinox seasonal bins, and 10% in June solstice. Even though the amount of GOCE data was significantly reduced, a sufficiently large number of data points (as shown in Figure 1 and Table 1) was still present to allow a meaningful statistical analysis of winds in the dawn and dusk sectors. Importantly, different sample populations and different sample population sizes were determined to not result in statistically different scientific results.

In the present study, we included wind data from ground-based stations that are above 45N MLAT. To stabilize the model fits, we included global wind data from all the three satellites included in this study. The entries in the "data points" column of Table 1 reflect the total number of data points used in this study. Figure 1 shows the spatial distribution of the selected data, as a function of magnetic latitude and local time and for each seasonal bin; it suggests that in winter and equinox, all magnetic latitudes and local times are sufficiently covered. On the other hand, in the summer season, the daytime sector has full data coverage, but there are substantial gaps in the nighttime sector. Daytime winds are primarily represented by the satellite observations and nighttime winds by ground-based FPIs, SDIs, and WINDII red line measurements.

3 Methodology for Model Development

Vector spherical harmonics (VSH) are appropriate basis functions [e.g., *Morse and Feshbach*, 1953; *Swarztrauber*, 1993; *Drob et al.*, 2008; *Emmert et al.*, 2008] to empirically model average quiet-time wind patterns for each seasonal bin. A VSH basis permits the continuous representation of a vector field on the surface of a sphere; the interpretation of the azimuthal degeneracy at the poles is discussed in *Emmert et al.* [2008]. VSH functions also facilitate the assimilation of single-component wind data (i.e., the projection of the wind vector along only one direction) such as from GOCE and DE2 WATS [e.g., *Emmert et al.*, 2010; *Drob et al.*, 2008, 2015]. Although this study is focused on the seasonal climatology of upper thermospheric winds only for magnetic latitudes above 45N, in our analysis, we have included global GOCE, DE2 WATS, and WINDII data to stabilize the global VSH fits.

The thermosphere is commingled with a weakly ionized plasma with an embedded magnetic field. The geomagnetic field naturally organizes ionospheric plasma motions, and ion drag is one of the primary drivers of neutral winds at high latitudes. As a result, high-latitude neutral winds are better organized in magnetic latitude and magnetic local time (MLT) than in geographic latitude and local time [*Richmond et al.*, 2003; *Emmert et al.*, 2008, 2010]. Accordingly, we constructed our model in Quasi-Dipole latitude and magnetic local time [*Richmond*, 1995; *Emmert et al.*, 2010]. This choice of coordinates alleviates the need for longitude or universal time (UT) terms in the model. Any UT dependence in the wind data is averaged out in our model, but the UT dependence of high-latitude winds is much smaller in magnetic coordinates than in geographic coordinates [*Emmert et al.*, 2010].

Based on physics-based model results and interpretation of individual datasets [e.g., *Meriwether*, 1983; *Killeen et al.*, 1986; *Niciejewski et al.*, 1996; *Conde and Smith*, 1998; *Emmert et al.*, 2006b], the characteristic features of the high latitude neutral wind circulation include sharp wind reversals at the equatorward edge of a thermospheric circulation cell on the duskside, strong antisunward winds over the polar cap, and a weaker tendency toward a dawnside circulation cell. The sharp wind reversals are associated with the interplay between ion drag and dayside solar heating pressure gradient forces on the fluid [*McCormac et al.*, 1987]; this produces strong latitudinal gradients in the zonal winds at the outer boundary of the auroral oval centered between 65N and 75N MLAT during quiet geomagnetic conditions. These strong gradients are a persistent feature of the neutral wind circulation at high latitude and are known for generating the thermosphere's most dynamic weather. The available data have sufficient high latitude data coverage in magnetic latitude and magnetic local time to accurately model these features with a VSH expansion at order 17 in magnetic latitude (=N) and wavenumber 5 in magnetic local time (=M). In terms of global gridpoint models, order 17 corresponds to a spatial resolution of $\sim$7 degrees in latitude [*Laprise*, 1992] and zonal wavenumber 5 corresponds to a temporal resolution of $\sim$2.4 hours in magnetic local time.

For each seasonal bin, we estimated the VSH coefficients via ordinary least squares. For quality control, any data point more than 3 standard deviations away from the initial fit was excluded from a subsequent and final fit. The models for each season were then evaluated as a function of magnetic latitude and local time on a regular grid and at the locations of the observations. Further, the VSH coefficients were used to calculate the divergence and vorticity in the winds (discussed in section 5.2).

4 Model Validation and Discussion

The model output and binned averages of the wind data used in its estimation are compared in this section to validate the modeled average variations in the winds. Two main criteria for model validation are 1) whether it adequately represents the salient features of the available data (following the criteria of *Emmert et al.* [2006a, section 3.1]) without overfitting or underfitting them, and 2) the model robustness in regions of limited data availability. In addition, because the datasets were collected from diverse instruments, we investigated for any biases that may exist among them. These validation results as a function of magnetic local time and magnetic latitude are detailed in sections 4.1 and 4.2. After assuring the satisfactory behavior of the modeled wind climatology within the limits of its resolution, the main scientific results of this study are discussed in sections 5.

4.1 Magnetic Local Time Dependence

To investigate the seasonal behavior of neutral winds as a function of magnetic local time, in the first step we sorted the quiet-time climatological output and observational data into the three seasonal bins (December Solstice, Equinox, and June Solstice), 5 degree MLAT and 1 hour MLT bins, and computed averages for each bin. Any data point more than 3 standard deviations away from the mean and any bin containing less than 5 data points were discarded. The bin-averaged winds are plotted as a function of MLT in Figures 2 and 3. The quiet-time climatological model was evaluated at the locations of observations, and then binned and averaged in the same way as the data (blue curve). Figures 2 and 3 also show model cuts along MLT at a specific MLAT.

Figures 2 and 3 show the binned-average winds from WINDII, WATS, FPIs (except Urbana and Peach Mountain), and SDIs. For the FPI data, wind components along the geographic cardinal directions are measured at different times. For these data, we first averaged the observed geographic wind components and then projected the average wind vectors along magnetic directions. For the Urbana (UR) and Peach Mountain (PM) FPI data, line-of-sight (LOS) winds along the geographic cardinal directions are measured; derived vector winds are not reported in the data. So for UR FPI and PM FPI, we used a different approach discussed later in this section.

There is a consistent progression of average winds from one bin to the next. The quiet-time winds from ground-based instruments and WINDII are in agreement with each other with few systematic discrepancies (discussed below). This suggests that overall there are no major biases among these datasets; they can be reasonably combined without correction. A few of the datasets, however, exhibit some regional differences with the fits and other data sets. In addition, the figures illustrate that the morphology of the binned-average high-latitude zonal and meridional winds is generally matched by the model (thus no underfitting).

WATS data is one exception here. For the datasets shown in Figures 2 and 3, both wind components (zonal and meridional) are available in geographic coordinates at common times, permitting computation of the wind components in magnetic coordinates. On the other hand, WATS only measured geographic zonal winds. Therefore, it is not possible to transform WATS winds to geomagnetic coordinates for bin-averaging purposes, although the data were assimilated into the model by projecting the vector basis functions along the geographic zonal direction [*Emmert et al.*, 2008]. The WATS data depicted in Figure 2 are longitudinally averaged geographic zonal winds binned in the same way as the other instruments. Thus, the comparison of WATS with the other data is not ideal. Although WATS zonal winds are in good agreement with all other datasets at the middle and lower auroral latitudes (< 65N MLAT), above 65N MLAT marked differences are present between them. The discrepancies between WATS and other datasets increase with increasing latitude; this suggests that these apparent discrepancies may be associated with the use of geographic coordinates for WATS zonal winds, given that the difference between geographic and geomagnetic zonal directions also increases with increasing latitude. Altitude and solar activity may also be contributing to the differences: Most of the WATS data included in our data assimilation lie near the upper limit (150 sfu) of the $F_{10.7}$ range (the average $F_{10.7}$ for WATS data is 135.6 sfu, as shown in Table 1), and near the upper limit of the altitude range.

Discrepancies between WINDII green line binned averages and modeled climatology occur above 75N MLAT on the dayside, where the model winds are significantly more eastward ($\sim$80 ms^{-1}) and northward ($\sim$80 ms^{-1} in the 75–80 MLAT bin and higher) than WINDII between 1200 and 1800 MLT. In this region (MLAT–MLT sector), a large quantity of GOCE cross-track wind data is present. Recently, *Conde* [2015] and *Kärräng* [2015] found that the GOCE cross-track wind observations are 1.2 to 2 times larger than ground-based measurements in both northern and southern high latitudes. Thus, this discrepancy may be skewing the fit away from the WINDII data. A detailed comparison between GOCE, WINDII, FPI, and SDI measurements is discussed in the next section. A discrepancy also exists between Søndrestrom FPI (SS FPI) and the Alaskan SDIs (Poker Flat and Toolik Lake) zonal winds during the winter and equinox seasons: The Sondrestrom winds are up to 100 ms^{-1} more westward than the Alaskan SDI winds. Although, the reasons for this apparent discrepancy are not immediately clear, the possible reason can be the the strength of magnetic field, the tilt of the magnetic field line, or widely separated magnetic longitudes of these stations.

In the 60–65N MLAT bin, the Poker Flat SDI meridional winds tend to be slightly more equatorward than the Toolik Lake SDI winds (Figure 3). Furthermore, in the 55–60N MLAT bin, the Millstone Hill (MH) FPI winds tend to be more equatorward than PF SDI. Finally, the WINDII red line meridional winds tend to be more equatorward than other datasets in December solstice. The reasons for these differences are not immediately clear; the average $F_{10.7}$ for all these datasets is similar (see Table 1), so different solar cycle sampling is not a likely cause.

The Millstone Hill, Urbana (UR), and Peach Mountain (PM) FPIs are at similar latitudes in a region of strong latitudinal gradients of the meridional winds [*Emmert et al.*, 2003]. To investigate the latitudinal gradients in more detail, we averaged north-looking and south-looking meridional winds (in the geographic direction) from these three stations, obtaining a total of six MLT profiles around middle latitudes. The results are shown in Figure 4, which indicates that, overall the modeled climatology is in a good agreement with the binned averages from these three middle latitude stations. The MLT dependencies of the geographic meridional wind are very similar: weaker and poleward in the dusk and dawn sectors, strongest and equatorward just after magnetic midnight. Strong latitudinal gradients are evident around 56N MLAT, but weaken with decreasing latitude. These features are consistent among the three seasonal bins, but the gradients appear to increase in strength from winter to summer. For MH FPI at northward observation location, the model climatology underestimated peak latitudinal gradient by $\sim$20 ms^{-1} in winter and $\sim$30 ms^{-1} in equinox. Figure 4 also shows geographic zonal winds from the three stations (east-looking and west-looking measurements are averaged together). The zonal winds are eastward on the duskside and westward on the dawnside, with the eastward-to-westward reversal occurring after magnetic midnight in winter and equinox, and around magnetic midnight in the summer season.

As can be seen in Figure 2, zonal winds exhibit a mainly semi-diurnal variation (4 extrema) at auroral latitudes, and a mainly diurnal variation (2 extrema) at lower latitudes. Near the pole, the wind components take on a diurnal character as a result of the azimuthal degeneracy. This diurnal behavior of zonal and meridional winds near the pole (as shown in Figures 2 and 3) is in agreement with *Wu et al.* [2008]. Zonal winds are stronger at polar latitudes than at the lower latitudes considered in this study. The semi-diurnal behavior of zonal winds at auroral latitudes is likely a consequence of the balance between ion drag and heating-driven winds. The meridional winds (Figure 3) exhibit a diurnal character at all latitudes (middle to polar).

Overall, at all the latitudes considered in this study, meridional winds are predominantly equatorward at nighttime (1800–0600MLT) and poleward during daytime (0600–1800 MLT). Their peak amplitude decreases with decreasing magnetic latitude. The strongest meridional winds occur in the polar cap (this is in agreement with *Killeen et al.* [1991]) and near midnight and noon, as expected from strong antisunward flows over the polar cap region, where ion drag and solar heating induced pressure gradients work in the same direction [*Killeen and Roble*, 1984; *Aruliah et al.*, 1996; *Deng and Ridley*, 2006]. They are strongest in the summer season with an average speed of $\sim$320 ms^{-1}.

4.2 Magnetic Latitude Dependence

Figures 5 and 6 show binned averages as a function of magnetic latitude (2 degree bins), for successive 2 hour magnetic local time bins. Averages and estimated uncertainties were computed as described in section 4.1, as were the superimposed model results. The morphology of the binned average high-latitude zonal and meridional winds is generally well matched by the model (exceptions are discussed below); this indicates that the model resolution is sufficient to capture the salient features in the data.

An interesting feature in the high latitude zonal winds is the presence of sharp latitudinal gradients on the duskside, peaking near 65N and 80N MLAT, with the westward extremum occurring in between. The modeled climatology is underestimating these strong auroral zone westward winds in the equinox and summer season that exist (based on WINDII green line data) for example in the 1400–2000 MLT bins (the reason for this discrepancy discussed in the following paragraph). The meridional wind averages indicate good agreement in latitude dependence among the ground-based FPIs and SDIs. In contrast, the WINDII red line meridional winds in winter, 1600–2400 MLT, 50–65N MLAT tend to be more southward than the ground-based data. A similar meridional wind discrepancy between the WINDII red line and other datasets is present in the December solstice 0400–0800 MLT sector at middle and auroral latitudes. The behavior of TL SDI meridional winds in the 1400–1600 MLT equinox bin is not consistent with WINDII green line and modeled winds; the TL SDI meridional winds in this case may be adversely affected by twilight conditions.

The discrepancies between the WATS zonal winds above 70N MLAT and other data, and between the WINDII red line data and ground-based FPI data, were discussed in section 4.1. Although the WINDII green line data follow the model closely at lower latitudes, above 75N MLAT there are deviations from the model on the dayside apparent in Figures 5 and 6, especially during the equinox and summer seasons. On the dayside (between 0800 and1600 MLT) above 75N MLAT, the only other contributing dataset is GOCE. WINDII green line data overlap with dense GOCE measurements as shown in Figure 1. The GOCE accelerometer (GOCE ACC) measured only cross-track winds, so it was not possible to include GOCE data in Figures 1–6. To investigate whether the GOCE data are the source of this discrepancy between WINDII green line and modeled wind, for each season we binned the data from each instrument in 2 degree MLAT bins and successive 1 hour MLT bins. The average vector winds from each bin were used to compute the average wind component for each instrument along the average GOCE cross-track direction. The corresponding modeled cross-track winds were also computed and superimposed. The results are shown in Figure 7. The average GOCE cross-track unit vector, oriented with magnetic north at the top of the page, is shown in the rightmost column of Figure 7. Similarly, Figure 8 shows the calculated cross-track winds for all the instruments and model as a function of magnetic local time (hourly) for successive 5 degree MLAT bins above 60N MLAT. The GOCE cross-track wind data have limited local time coverage (mostly covering the dusk and dawn sector as shown in Figure 1), so only bins with GOCE data are shown in Figure 7 and Figure 8. In these figures (7 and 8), we restricted the GOCE data to only below 88N MLAT and between 0600 and 1900 MLT to avoid confusion among unit vector components near the pole.

Due to the near sun-synchronous dusk-dawn orbit, positive GOCE cross-track winds are generally in the anti-sunward direction, shifted slightly (up to 1.5 hours) in the post-midnight direction. In terms of zonal and meridional components, cross-track winds approximately represent eastward winds on the duskside, westward winds on the dawnside, and poleward winds near noon MLT. The average GOCE unit vector direction illustrates that the GOCE cross-track winds in the dusk and dawn sectors are virtually zonal and slowly turns into meridional around noon.

As shown in Figures 7 and 8, WINDII, SDI, and FPI measurements are generally consistent with each other (except WINDII red line between 0600 and1200 MLT in winter). The largest discrepancies between GOCE and other datasets exist on the duskside; they increase with increasing latitude. On the other hand, the agreement between GOCE and other data sets is much better on the dawnside. Overall, GOCE cross-track winds on the duskside are more positive than the winds measured by other stations (Figure 7). GOCE cross-track winds on the duskside (16–19 MLT region) are 89 ms^{-1}, 73 ms^{-1}, and 87 ms^{-1} stronger (positive) on the average than WINDII green line cross-track winds in winter, equinox, and summer, respectively. Despite this offset, the GOCE data clearly shows the signature of the wind reversal in the duskside circulation cell at around 75N MLAT in Figure 7.

The modeled cross-track winds are in better agreement with ground-based (FPI and SDI) and WINDII data in December solstice and equinox, whereas they are in good agreement with the GOCE data in June solstice. This is the result of including a larger GOCE data fraction in the model fits for June solstice (10%) compared to December solstice (3.3%) and equinox (3.3%), combined with the scarcity of ground-based high-latitude data in summer. Figure 8 shows that in the 1600–2000 MLT sector, the GOCE data are skewing the fit away from the WINDII data (especially in the summer). The fitted cross-track winds are more positive (eastward) than WINDII green line data and this result reflects in Figures 2 and 5. In the 75–85 MLAT and 1200–1600 MLT region in equinox and summer, the model is fitting GOCE data better than the WINDII green line data (Figure 8) and as a result the modeled cross-track winds are more positive than WINDII. Because the GOCE winds are virtually close to meridional at these latitudes and local times, (as shown by the average direction of the unit vector), they contribute strongly towards the poleward component of the modeled wind at these latitudes and local times, which explains the observed discrepancy between the WINDII green line and modeled meridional winds (shown in Figures 3 and 6) at 75–85 MLAT and 1200–1600 MLT in equinox and summer. Figures 7 and 8 illustrate significant differences in the polar cap stations (TH FPI and RB FPI) and GOCE cross-track winds.

Liu et al. [2016] studied the seasonal variation of quiet time thermospheric winds below 50N magnetic latitude using GOCE data and found that HWM14 underestimates the eastward winds around dusk by $\sim$20 ms^{-1} compared to GOCE. In the current study, as discussed above, we found discrepancies between GOCE and other datasets. On the duskside, GOCE winds are more eastward (apparently around middle latitudes) compared to all other datasets as shown in Figures 7 and 8. This suggests that such GOCE discrepancies may be present at lower latitudes as well and may explain the low-latitude differences between GOCE and HWM14 noted by *Liu et al.* [2016].

Possible causes of error in the GOCE wind data are 1) calibration errors in the accelerometer data, 2) errors in the radiation pressure model, used to reduce the accelerometer measurements to aerodynamic drag and lift accelerations, and 3) errors in the GOCE aerodynamic model parameters that influence the lift over drag ratio. None of these error sources would likely result in crosswind errors on the duskside only. The relative contributions of the first two error sources are reduced when the aerodynamic acceleration signal increases, with lower altitude or higher drag. Yet, no significant systematic changes to the wind observations are observed over the lifetime of the mission, which started at higher altitudes and low solar activity, and ended at lower altitudes and higher solar activity. So the most likely error source is the aerodynamic modelling of GOCE, which might include influences due to geometry modelling errors and uncertainties in the gas-surface interaction parameters. This is currently undergoing detailed investigation.

Finally, the discrepancy between GOCE and the other data might be a result of the different nature of the observations. The GOCE observations are instantaneous and well-localized "in-situ" measurements, while the FPI, SDI and UARS WINDII observations represent wind conditions over a certain height range of emissions and during an observation time interval of several minutes (line-of-sight integrated measurement). Another reason for GOCE discrepancy might be associated with the intense ionospheric variations that results in a very dynamic drag environment [*Ince and Pagiatakis*, 2016]. In general, such variations should disappear in the binning and averaging process, but perhaps there is a poorly understood aspect of the wind distribution at play here.

5 Results and Discussion

This section investigates the large scale seasonal behavior of the modeled average winds as a function of magnetic latitude and local time. The seasonal variation in calculated vorticity and divergence of the modeled horizontal wind field is also discussed here.

5.1 Seasonal Dependence

Figure 9 shows the average F-region assimilated neutral vector winds for the winter, summer, and equinox seasons (as seen by a space-based observer located some distance above the geomagnetic north pole). Background colors represent the strength of horizontal neutral winds. Visual inspection of Figure 9 illustrates the well-known characteristic features of high latitude thermospheric wind circulation; for example, a strong and large duskside circulation cell, a weaker tendency towards a dawnside circulation cell, sharp latitudinal gradients due to the wind reversals that exist in the duskside auroral zone, and strong antisunward winds in the polar cap. In all the seasons, the mean horizontal neutral wind field is dominated by rotational flow. The most visible effect of season on the neutral wind circulation shown in Figure 9 is a progressive intensification of wind patterns from December solstice to equinox to June solstice.

During the summer season, the polar geospace environment (geomagnetic polar cap and auroral latitudes) receives continuous solar illumination, which results in generally higher ionospheric plasma density in summer than in winter, except at certain UTs [*Sojka et al.*, 1982]. In the summer season, the ionospheric plasma is dominated by locally generated plasma. Auroral energetic particle precipitation also enhances the local plasma density and ionospheric conductivity [*Kwak and Richmond*, 2007]. *Liou et al.* [2001] investigated the seasonal dependence of auroral precipitation and showed that nighttime auroral precipitation is stronger in the winter, and daytime auroral precipitation is stronger in the summer; *Lee and Shepherd* [2007] found the precipitating energy flux to increase with increasing solar zenith angle from 40 to 160 degree. *Ridley* [2007] suggested that at auroral latitudes, the conductance associated with auroral energetic particle precipitation (auroral conductance) dominates on the nightside over the conductance associated with ionization caused by solar radiation (solar driven conductance). Also, due to the nature of plasma convection trajectories, the plasma produced by solar ionization on the dayside is transported to the nightside [*Fuller-Rowell et al.*, 1988]. This means there is always enough plasma, at least around auroral latitudes, to drive nightside thermospheric circulation via ion-neutral coupling (see Figure 1 of *Kwak and Richmond* [2007]). This is likely the reason for the visible ion drag effect at auroral latitudes on the nightside in the winter season despite the low solar produced plasma. In addition, the seasonal interplay between the auroral conductance, solar driven conductance, and plasma transported from the dayside to nightside is possibly the cause of differences in the wind circulation patterns shown in Figure 9.

A summary of direct seasonal comparisons between the winter solstice, equinox, and summer solstice winds as a function of magnetic local time at various latitudes is presented in Figure 10. Figure 11 illustrates seasonal maps of high latitude zonal and meridional winds as a function of magnetic latitude and magnetic local time. Together, they (Figures 9–11) completely illustrate the seasonal changes in high latitude thermospheric wind behavior. On average, winds are strongest in summer and weakest in winter. Antisunward winds in the polar cap show strong seasonal dependence; their magnitude increases from winter to summer. In the polar cap, although both ion drag and solar heating induced pressure gradients produced by dayside heating work in the same direction (antisunward), antisunward winds are driven primarily by the solar pressure gradients; the ion drag forcing on the neutral winds maximizes in the sunward ion flows on the duskside and dawnside [*Killeen and Roble*, 1984]. The neutral wind thermal forcing associated with solar heating changes with the change in seasons due to the movement of the solar terminator with seasons. The seasonal dependence of the thermal forcing may therefore be responsible for the seasonal behavior of polar cap antisunward winds, but it not possible to tell from the wind observations alone the relative contributions of ion drag and thermal forcing.

As shown in Figures 9–11, at all latitudes, zonal winds are generally strongest between 0000 and 1500 MLT in the summer and weakest in the winter. A similar trend is present in zonal winds between 2000 and 2400 MLT at and above auroral latitudes (MLAT > 60N). In contrast, between 1800 and 2400 MLT below auroral latitudes, winter zonal winds are strongest and summer zonal winds are weakest. Even though there are some offsets among the modeled winds and constituent datasets, the individual datasets support the seasonal dependences discussed above. These results also agree with the climatological study by *Emmert et al.* [2006b].

On the duskside at the equatorward boundary of the auroral oval, the momentum transferred to neutrals by ions via ion drag is largely balanced by the dayside solar heating induced pressure gradient forces [*Killeen and Roble*, 1986]. Ion drag on the duskside works in the same sense as the Coriolis force, which combines with ion drag to counteract the pressure gradients. The interplay between the ion drag driven westward flows and heating induced pressure gradient driven antisunward flows result in a shear boundary in the auroral zonal winds on the duskside [*McCormac et al.*, 1987; *Dhadly et al.*, 2015], as shown in Figures 9–11. The shear boundary moves to lower latitudes with increasing magnetic local solar time in all three seasons. It appears at earlier MLTs in summer and equinox compared to winter, whereas it disappears later in winter than summer (as shown in Figure 9). The strength of zonal winds channeling through the auroral zone around 70 MLAT between 1800 and 2400 MLT is strongest in the summer season. This wind channel formation at auroral latitudes is primarily the consequence of auroral precipitation that usually enhances the local plasma density at auroral latitudes, strengthening the momentum transfer between ions and and neutrals [*Killeen et al.*, 1991; *Deng and Ridley*, 2006]. Although there are some discrepancies between the WINDII green line and modeled winds in this region due to the influence of GOCE cross-track data as discussed in the previous section, WINDII green line data support this seasonal trend. In the June solstice and equinox cases, the WINDII data indicate stronger sunward flows than modeled on the equatorward side of the dusk cell (Figure 5).

On the dawnside, the cross-flow deflection of the Coriolis force is opposite to the sense of curvature of the dawn-side ion-drag cell; this limits the ability of neutrals to become entrained in the dawn circulation cell [*Fuller-Rowell*, 1984; *Killeen and Roble*, 1984; *Deng and Ridley*, 2006] as shown in Figure 9. The appearance of a small eastward component in auroral (and even lower latitude) zonal winds after magnetic midnight between 0000 and 0500 MLT (as shown in Figures 9–11) is likely due to the influence (via ion drag) of the dawnside plasma circulation cell; this slight cyclonic tendency in neutral winds diminishes from winter to summer. This suggests that the combination of Coriolis force and pressure gradients in the summer may be dominating ion drag on the dawnside.

Figure 10 illustrates that the sign of the zonal and meridional winds as a function of MLT has a seasonal variation. On the nightside, in general, zonal winds turn westward progressively earlier from summer to winter. In contrast, there is no such clear trend in the time of west-to-east reversals on the day side. At auroral latitudes (above 65N MLAT), summer zonal winds remain westward at all local times. Similar directional changes are present in the meridional winds at polar and middle latitudes: Meridional winds turn equatorward progressively earlier from summer to winter on the duskside, but there is no clear seasonal dependence of the equatorward-to-poleward reversal time on the dawnside. Figure 4 and Figure 10 illustrate that the zonal winds at auroral and middle latitudes become more westward from winter to summer at all local times. Similarly, the meridional winds at middle latitudes become more equatorward from winter to summer at all local times.

5.2 Vorticity and Divergence

A horizontal wind field may be decomposed into the vertical component of vorticity and the horizontal divergence (divergence of the horizontal wind components). Vertical vorticity is the measure of shears or any curvature present in the horizontal wind flows, whereas divergence of the horizontal wind is usually associated with vertical motions induced by heating or cooling of thermospheric air. For simplicity, here vertical vorticity is referred to as vorticity and horizontal divergence as divergence. At high latitudes, thermospheric vorticity is primarily driven by ion drag and divergence by heating induced pressure gradients [e.g., *Mayr and Harris*, 1978; *Volland*, 1979; *Hays et al.*, 1984; *Thayer and Killeen*, 1991, 1993; *Förster et al.*, 2011; *Kwak and Richmond*, 2014]. An advantage of using VSH representation is that the vorticity and divergence of the average wind field can be computed from the coefficients of the empirical quiet-time model [e.g., *Swarztrauber*, 1993]. Figure 12 and Figure 13 illustrate the resulting seasonal dependence of vorticity and divergence patterns. Positive vorticity represents cyclonic rotation (anticlockwise in the Northern Hemisphere) and negative vorticity represents anticyclonic rotation (clockwise in the Northern Hemisphere). Positive divergence represents divergence and negative values represent convergence. Calculated minimum and maximum values of divergence and vorticity for each season are printed at the bottom of each season panel.

Figure 12 clearly illustrates the formation of the well-known high latitude thermospheric duskside anticyclonic and dawnside cyclonic vorticity cells and their seasonal dependence. In the winter and equinox seasons, the high latitude thermospheric circulation splits into two vortices: anticyclonic in the duskside and cyclonic in the dawnside. In comparison, in summer the dawnside vortex is less well defined. Unfortunately, in the summer season, there are virtually no data from any data station in 0100–0500 MLT sector above 56N MLAT to define the vorticity. The general behavior of these vorticity maps is in agreement with the patterns deduced from DE2 discussed in *Thayer and Killeen* [1991]. In the winter and equinox season, dusk and dawnside vorticity patterns are virtually aligned with the noon-midnight meridian. In each season, the maximum anticyclonic vorticity occurs in the dusk sector, whereas the maximum cyclonic vorticity occurs in the dawn sector. Vorticity is zero when either the wind field is uniform or shears reverse their direction. Thus, the strong latitudinal vorticity gradients on the duskside at auroral latitudes coincide with the wind shears seen in Figure 9. The contour of zero vorticity in the dusk sector stays above 60N MLAT and indicates only a slight change in location with the change in season; this suggests that the latitudinal extent of the duskside circulation cell does not depend strongly on season. However, vorticity in the dusk sector increases dramatically from winter to summer, with peak anticyclonic magnitude of 218×10^{-6} s^{-1} in winter and 647×10^{-6} s^{-1} in summer. The dawnside vorticity vortex changes shape with the change in season; its latitudinal extent increases slightly from winter to equinox. There is no dramatic variation in the peak cyclonic vorticity with the change in season; it varies only between 136×10^{-6} s^{-1} (equinox) and 168×10^{-6} s^{-1} (winter). The averages of absolute vorticity over the entire region shown in Figure 12 in winter, equinox, and summer season are 54×10^{-6} s^{-1}, 58×10^{-6} s^{-1}, and 108×10^{-6} s^{-1} respectively. This indicates overall increase in vorticity from winter to summer.

Ion-neutral momentum coupling is the key source for driving high latitude thermospheric vorticity [*Kwak and Richmond*, 2014]. The increase in vorticity from winter to summer suggests an increase in momentum exchange between ions and neutrals and hence increasing ionosphere-thermosphere coupling from winter to summer, most likely associated with higher summer plasma densities that result from increased photoionization.

Figure 13 illustrates the changes in divergence with the change in season and formation of multiple small islands. Divergence fields in all the three seasons are more complex than their corresponding vorticity fields. The seasonal divergence comparison indicates that the strongest divergences occur primarily in and above auroral latitudes (MLAT $>$ 65N), in regions which are most likely associated with the high latitude local heating sources such as Joule heating and heating due to particle precipitation. The average of absolute divergences over the entire region shown in Figure 13 in winter, equinox, and summer season are 37×10^{-6} s^{-1}, 60×10^{-6} s^{-1}, and 52×10^{-6} s^{-1} respectively. Divergence is thus largest in equinox and smallest in winter.

There is a consistent region of strong divergence just after magnetic local noon (1200–1400 MLT) between 70 and 80N MLAT. This divergence feature is present in all three seasons and is strongest in equinox. The location of this divergence region is in the vicinity of magnetospheric cusp region and matches closely with the locations of the quiet-time thermospheric neutral mass density enhancement in the polar region observed by CHAMP ($\sim$400 km) [*Liu et al.*, 2005]. Thermospheric density enhancement in the geomagnetic cusp is a persistent feature of the thermospheric neutral density field and was observed virtually during all the CHAMP cusp passes [*Lühr et al.*, 2004; *Liu et al.*, 2005]. Local divergence near the mass density anomaly is probably required to produce the anomaly. This divergence feature thus may be a signature of localized cusp heating.

In each season discussed here, divergence is weaker than vorticity. This result is also consistent with other large scale climatological studies [e.g., *Thayer and Killeen*, 1991; *Kwak and Richmond*, 2014] and local climatologies at auroral latitudes [*Dhadly and Conde*, 2016]. The thermosphere is convectively stable because of its positive temperature gradient and hence opposes vertical mass transport [*Dhadly and Conde*, 2016] that would lead to horizontal divergence. Gravity waves can generate substantial but localized and short lived divergences that are possibly larger than the vorticity. Because they are localized, short lived, traveling, and do not appear repeatedly at any predictable location, so they would average out in large-scale climatological studies like this.

6 Conclusions

This study provided the first empirical determination of the large scale seasonal response of quiet-time (K_p $<$ 3 and $80 \leq F_{10.7} \leq 150$) high latitude F-region thermospheric horizontal neutral winds in magnetic coordinates. Extensive daytime and nighttime observations of upper thermospheric winds recorded by 11 ground-based (optical remote sensing) and space-based (optical remote sensing and in situ) instruments at a variety of northern high latitudes were combined. They provided enough seasonal, latitudinal, and local time coverage at all the northern high latitudes to accurately develop a new empirical description of climatological quiet-time winds as a function of season, latitude, and local time in magnetic coordinates.

The comparison among the various datasets in this effort indicated that WINDII, SDI, and FPI observations are generally consistent with each other. Some minor systematic offsets exist among these datasets, mainly in the meridional direction; however, the magnetic local time and latitude dependences are in very good agreement. Larger discrepancies exist between GOCE winds and the other datasets; these discrepancies are strongest on the duskside, where the GOCE cross-track winds are $\sim$70–90 ms^{-1} more positive (left to right relative to the GOCE direction of motion) than the other datasets. The discrepancies between the modeled wind and WINDII green line are stronger at the locations where GOCE data is present. In general, the empirical model represents the average of the datasets, but is slightly skewed toward GOCE when there are few other data available.

Even though some discrepancies exist between various datasets, the overall morphology of the high-latitude winds is consistent among the datasets and the empirical model of the data (in geomagnetic coordinates). The assimilated winds verify several well-known characteristic features of high latitude thermospheric circulation: a strong and large duskside anticyclonic circulation cell, sharp latitudinal gradients (shears) due to the wind reversals that exist in the auroral zone, strong antisunward winds in the polar cap, and a weaker tendency toward a dawnside cyclonic circulation cell.

The large scale seasonal dependence of high-latitude wind patterns, which until now has received little attention, is quite pronounced. The mean neutral wind circulation is strongest in the summer season and weakest in the winter season. The magnetic local time dependence of the zonal wind component shows a mainly semi-diurnal character (4 extrema) at auroral latitudes, and a mainly diurnal variation (2 extrema) at lower latitudes. In contrast, the meridional winds predominantly exhibit a diurnal character at all latitudes considered in this study. Near the pole, both wind components take on a purely diurnal character as a result of the azimuthal degeneracy in the region of uniform antisunward flow. At auroral latitudes, zonal winds form a channel of strong westward flows on the duskside. The strength of zonal winds channeling through the auroral zone on the duskside is strongest in the summer season. This wind channel formation at auroral latitudes is primarily the consequence of auroral precipitation that usually enhances the local plasma density and strengthens the momentum transfer between ions and and neutrals. The occurrence of eastward winds in auroral (and lower) latitude zonal winds between 0200 and 0500 MLT is likely due to the influence (via ion drag) of the dawnside plasma circulation cell. This slight cyclonic tendency in the winds that appears between 0200 and 0500 MLT diminishes from winter to summer.

Local time evolution of the duskside shears shows that, in all the seasons, the shear boundary moves to lower latitudes with increasing magnetic local solar time. The shear boundary appears at earlier local times in summer and equinox compared to winter, whereas it disappears later in winter than summer. Also, the direction of zonal winds as a function of MLT shows seasonal variation. On the night side, in general, zonal winds turn westward progressively earlier from summer to winter. In contrast, there is no such clear trend in the time of west-to-east reversals on the day side. At auroral latitudes (above 65N MLAT), summer time zonal winds remain westward at all local times. Zonal winds at auroral and middle latitudes become more westward from winter to summer at all local times. Overall, the westward zonal winds at auroral and middle latitude are strongest in summer and weakest in winter.

Furthermore, meridional winds are predominantly equatorward at nighttime (1800–0600 MLT) and poleward during daytime (0600–1800 MLT). Their peak amplitude decreases with decreasing magnetic latitude. Meridional winds turn equatorward earlier in summer than winter on the duskside, but there is no clear seasonal dependence of the equatorward-to-poleward reversal time on the dawnside. The meridional winds at middle latitudes become more equatorward from winter to summer at all local times. At middle latitude sites, the nighttime meridional wind latitudinal gradient increases from winter to summer.

Vorticity and divergence present in the northern high latitude thermospheric winds also show seasonal dependences. Overall, the vorticity and divergence increase from winter to summer, suggesting an increase in ionosphere-thermosphere coupling from winter to summer. The peak anticyclonic vorticity (duskside cell) increases more dramatically from winter to summer than the peak cyclonic vorticity (dawnside cell). The latitudinal extent of the duskside circulation cell does not depend strongly on season.

In all the seasons, the strongest divergences occur primarily in and above auroral latitudes (MLAT $>$ 65N), in regions which are most likely associated with the high latitude local heating sources such as Joule heating and heating due to particle precipitation. There is a consistent region of strong divergence just after magnetic local noon (1200–1400 MLT) between 70 and 80N MLAT, which is near the magnetic cusp; this feature is strongest during equinox. The location of this divergence region is close to observed neutral mass density enhancements at ∼400 km altitude, suggesting that it may be related to localized cusp heating. In all the seasons, divergence is weaker than vorticity.

In a future paper, we will examine the dependence of the extensive high-latitude wind measurements on the configuration of the interplanetary magnetic field. HWM has rudimentary low order representation of these effects. This work will be folded into future versions of HWM to improve its performance at high latitudes.

Acknowledgments

This study was supported by NASA's Heliophysics Supporting Research Program (grant NNH16AC38I). This work was conducted while Manbharat Singh Dhadly held a National Research Council's Research Associateship at Naval Research Laboratory, Washington, DC. K_p and $F_{10.7}$ indexes are available at NASA OMNIWeb data explorer (http://omniweb.gsfc.nasa.gov/form/dx1.html). Poker Flat and Toolik Lake SDI data are available at http://sdi_server.gi.alaska.edu/sdiweb/index.asp. WINDII Level 2 data are available from Gordon Shepherd (gordon@yorku.ca). GOCE data can be obtained from https://earth.esa.int/web/guest/missions/esa-operational-missions/goce /goce-%20thermospheric-data. DE2 WATS data are available at ftp://spdf.gsfc.nasa.gov/pub/data/de/de2 /combined_plasma_neutrals_ua/ua_atmoweb/. All other data sets can be obtained from the Madrigal database at http://cedar.openmadrigal.org/cgi-bin/accessData.cgi. Poker Flat and Toolik Lake SDI operations (during the observing periods included in this manuscript) were supported by the National Science Foundation through grant numbers AGS1243476, AGS1140075, and AGS0821431. Resolute Bay data was supported by the National Science Foundation through grant AGS1339918. For Peach Mountain and Urbana FPIs, work at the University of Illinois was supported by the National Science Foundation through grant AGS 14-52291.

References

Anderson, C., M. Conde, and M. G. McHarg (2012), Neutral thermospheric dynamics observed with two scanning Doppler imagers: 1. Monostatic and bistatic winds, *J. Geophys. Res. Sp. Phys.*, *117*(A3), A03,304, doi:10.1029/2011ja017041.

Aruliah, A. L., D. Rees, and T. J. Fuller-Rowell (1991a), The combined effect of solar and geomagnetic activity on high latitude thermospheric neutral winds. Part I. Observations, *J. Atmos. Terr. Phys.*, *53*(6–7), 467–483, doi:http://dx.doi.org/10.1016/0021-9169(91)90075-I.

Aruliah, A. L., D. Rees, and A. Steen (1991b), Seasonal and solar cycle variations in high- latitude thermospheric winds, *Geophys. Res. Lett.*, *18*(11), 1983–1986, doi: 10.1029/91GL02240.

Aruliah, A. L., A. D. Farmer, D. Rees, and U. Brändström (1996), The seasonal behavior of high-latitude thermospheric winds and ion velocities observed over one solar cycle, *J. Geophys. Res.*, *101*(A7), 15,701, doi:10.1029/96JA00360.

Babcock, R. R., and J. V. Evans (1979), Seasonal and solar cycle variations in the thermospheric circulation observed over Millstone Hill, *J. Geophys. Res.*, *84*(A12), 7348, doi:10.1029/JA084iA12p07348.

Buonsanto, M. J., Y. K. Tung, and D. P. Sipler (1992), Neutral atomic oxygen density from nighttime radar and optical wind measurements at Millstone Hill, *J. Geophys. Res.*, *97*(A6), 8673, doi:10.1029/92JA00435.

Conde, M. (2015), Comparison between thermospheric winds measured by a ground-based Fabry-Perot spectrometer at Mawson, Antarctica, and winds determined in-situ from satellite drag, *Am. Geophys. Union Fall 2015*, (SA33A-07).

Conde, M., and R. W. Smith (1995), Mapping thermospheric winds in the auroral zone, *Geophys. Res. Lett.*, *22*(22), 3019–3022, doi:10.1029/95GL02437.

Conde, M., and R. W. Smith (1998), Spatial structure in the thermospheric horizontal wind above Poker Flat, Alaska, during solar minimum, *J. Geophys. Res.*, *103*(A5), 9471–9949, doi:10.1029/97JA03331.

Deng, Y., and A. J. Ridley (2006), Dependence of neutral winds on convection E-field, solar EUV, and auroral particle precipitation at high latitudes, *J. Geophys. Res. Sp. Phys.*, *111*(A9), A09,306, doi:10.1029/2005JA011368.

Dhadly, M. S., and M. Conde (2016), Distortion of thermospheric air masses by horizontal neutral winds over Poker Flat Alaska measured using an all-sky scanning Doppler imager, *J. Geophys. Res. Sp. Phys.*, *121*(1), 854–866, doi:10.1002/2015JA021800.

Dhadly, M. S., J. Meriwether, M. Conde, and D. Hampton (2015), First ever cross comparison of thermospheric wind measured by narrow- and wide-field optical Doppler spectroscopy, *J. Geophys. Res. Sp. Phys.*, *120*(11), 9683–9705, doi: 10.1002/2015JA021316.

Doornbos, E. (2011), Thermospheric Density and Wind Determination from Satellite Dynamics, Ph.D. thesis, University of Delft.

Doornbos, E., S. Bruinsma, B. Fritsche, P. Visser, J. Van Den IJssel, J. T. Encarnacao, and M. Kern (2013), Air Density And Wind Retrieval Using GOCE Data, *ESA Living Planet Symp. Proc. Conf. held 9-13 Sept. 2013 Edinburgh United Kingdom. ESA SP-722. 2-13, p.7*, *722*, 7.

Doornbos, E. N., S. L. Bruinsma, B. Fritsche, G. Koppenwallner, P. Visser, J. Van Den IJssel, and J. Teixeira da Encarnação (2014), GOCE+ Theme 3: Air density and wind retrieval using GOCE data final report, *Tech. Rep.*(4000102847/NL/EL, TU Delft, Netherlands).

Drob, D. P., J. T. Emmert, G. Crowley, J. M. Picone, G. G. Shepherd, W. Skinner, P. Hays, R. J. Niciejewski, M. Larsen, C. Y. She, J. W. Meriwether, G. Hernandez, M. J. Jarvis, D. P. Sipler, C. . Tepley, M. S. O'Brien, J. R. Bowman, Q. Wu, Y. Murayama, S. Kawamura, I. M. Reid, and R. Vincent (2008), An empirical model of the Earth's horizontal wind fields: HWM07, *J. Geophys. Res. Sp. Phys.*, *113*(12), 1–18, doi:10.1029/2008JA013668.

Drob, D. P., J. T. Emmert, J. W. Meriwether, J. J. Makela, E. Doornbos, M. Conde, G. Hernandez, J. Noto, K. A. Zawdie, S. E. McDonald, J. D. Huba, and J. H. Klenzing (2015), An update to the Horizontal Wind Model (HWM): The quiet time thermosphere, *Earth Sp. Sci.*, *2*, doi:10.1002/2014EA000089.

Emmert, J. T., B. G. Fejer, C. G. Fesen, G. G. Shepherd, and B. H. Solheim (2001), Climatology of middle- and low-latitude daytime F region disturbance neutral winds measured by Wind Imaging Interferometer (WINDII), *J. Geophys. Res.*, *106*(A11), 24,701, doi:10.1029/2000JA000372.

Emmert, J. T., B. G. Fejer, G. G. Shepherd, and B. H. Solheim (2002), Altitude dependence of middle and low-latitude daytime thermospheric disturbance winds measured by WINDII, *J. Geophys. Res. Sp. Phys.*, *107*(A12), SIA 19–1–SIA 19–15, doi: 10.1029/2002JA009646.

Emmert, J. T., B. G. Fejer, and D. P. Sipler (2003), Climatology and latitudinal gradients of quiet time thermospheric neutral winds over Millstone Hill from Fabry-Perot interferometer measurements, *J. Geophys. Res.*, *108*(A5), 1196, doi:10.1029/2002JA009765.

Emmert, J. T., B. G. Fejer, G. G. Shepherd, and B. H. Solheim (2004), Average nighttime F region disturbance neutral winds measured by UARS WINDII: Initial results, *Geophys. Res. Lett.*, *31*(22), L22,807, doi:10.1029/2004GL021611.

Emmert, J. T., G. Hernandez, M. J. Jarvis, R. J. Niciejewski, D. P. Sipler, and S. Vennerstrom (2006a), Climatologies of nighttime upper thermospheric winds measured by ground-based Fabry-Perot interferometers during geomagnetically quiet conditions: 2. High-latitude circulation and interplanetary magnetic field dependence, *J. Geophys. Res.*, *111*(A12), A12,303, doi:10.1029/2006JA011949.

Emmert, J. T., M. L. Faivre, G. Hernandez, M. J. Jarvis, J. W. Meriwether, R. J. Niciejewski, D. P. Sipler, and C. A. Tepley (2006b), Climatologies of nighttime upper thermospheric winds measured by ground-based Fabry-Perot interferometers during geomagnetically quiet conditions: 1. Local time, latitudinal, seasonal, and solar cycle dependence, *J. Geophys. Res.*, *111*(A12), A12,302, doi:10.1029/2006JA011948.

Emmert, J. T., D. P. Drob, G. G. Shepherd, G. Hernandez, M. J. Jarvis, J. W. Meriwether, R. J. Niciejewski, D. P. Sipler, and C. A. Tepley (2008), DWM07 global empirical model of upper thermospheric storm-induced disturbance winds, *J. Geophys. Res.*, *113*(A11), A11,319, doi:10.1029/2008JA013541.

Emmert, J. T., a. D. Richmond, and D. P. Drob (2010), A computationally compact representation of Magnetic-Apex and Quasi-Dipole coordinates with smooth base vectors, *J. Geophys. Res.*, *115*(A8), A08,322, doi:10.1029/2010JA015326.

Fejer, B. G., J. T. Emmert, G. G. Shepherd, and B. H. Solheim (2000), Average daytime F region disturbance neutral winds measured by UARS: Initial results, *Geophys. Res. Lett.*, *27*(13), 1859–1862, doi:10.1029/2000GL003787.

Fejer, B. G., J. T. Emmert, and D. P. Sipler (2002), Climatology and storm time dependence of nighttime thermospheric neutral winds over Millstone Hill, *J. Geophys. Res.*, *107*(A5), 1052, doi:10.1029/2001JA000300.

Förster, M., S. Rentz, W. Köhler, H. Liu, and S. E. Haaland (2008), IMF dependence of high-latitude thermospheric wind pattern derived from CHAMP cross-track measurements, *Ann. Geophys.*, *26*(6), 1581–1595, doi:10.5194/angeo-26-1581-2008.

Förster, M., S. E. Haaland, and E. Doornbos (2011), Thermospheric vorticity at high geomagnetic latitudes from CHAMP data and its IMF dependence, *Ann. Geophys.*, *29*(1), 181–186, doi:10.5194/angeo-29-181-2011.

Fuller-Rowell, T. J. (1984), A two-dimensional, high-resolution, nested-grid model of the thermosphere: 1. Neutral response to an electric field “spike”, *J. Geophys. Res.*, *89*(A5), 2971, doi:10.1029/JA089iA05p02971.

Fuller-Rowell, T. J., D. Rees, S. Quegan, R. J. Moffett, and G. J. Bailey (1988), Simulations of the seasonal and universal time variations of the high-latitude thermosphere and ionosphere using a coupled, three-dimensional, model, *Pure Appl. Geophys. PAGEOPH*, *127*(2-3), 189–217, doi:10.1007/BF00879811.

Fuller-Rowell, T. J., M. V. Codrescu, H. Rishbeth, R. J. Moffett, and S. Quegan (1996), On the seasonal response of the thermosphere and ionosphere to geomagnetic storms, *J. Geophys. Res.*, *101*(A2), 2343, doi:10.1029/95JA01614.

Gault, W. A., G. Thuillier, G. G. Shepherd, S. P. Zhang, R. H. Wiens, W. E. Ward, C. Tai, B. H. Solheim, Y. J. Rochon, C. McLandress, C. Lathuillere, V. Fauliot, M. Hersé, C. H. Hersom, R. Gattinger, L. Bourg, M. D. Burrage, S. J. Franke, G. Hernandez, A. Manson, R. Niciejewski, and R. A. Vincent (1996), Validation of O(1 S) wind measurements by WINDII: the WIND Imaging Interferometer on UARS, *J. Geophys. Res. Atmos.*, *101*(D6), 10,405–10,430, doi:10.1029/95JD03352.

Hays, P. B., T. L. Killeen, N. W. Spencer, L. E. Wharton, R. G. Roble, B. A. Emery, T. J. Fuller-Rowell, D. Rees, L. A. Frank, and J. D. Craven (1984), Observations of the dynamics of the polar thermosphere, *J. Geophys. Res. Sp. Phys.*, *89*(A7), 5597–5612, doi:10.1029/JA089iA07p05597.

Hedin, A., E. Fleming, A. Manson, F. Schmidlin, S. Avery, R. Clark, S. Franke, G. Fraser, T. Tsuda, F. Vial, and R. Vincent (1996), Empirical wind model for the upper, middle and lower atmosphere, *J. Atmos. Terr. Phys.*, *58*(13), 1421–1447, doi:10.1016/0021-9169(95)00122-0.

Hernandez, G., and R. G. Roble (1976), Direct measurements of nighttime thermospheric winds and temperatures, 1. Seasonal variations during geomagnetic quiet periods, *J. Geophys. Res.*, *81*(13), 2065–2074, doi:10.1029/JA081i013p02065.

Ince, E. S., and S. D. Pagiatakis (2016), Effects of space weather on GOCE electrostatic gravity gradiometer measurements, *J. Geod.*, pp. 1–15, doi:10.1007/s00190-016-0931-8.

Kärräng, P. (2015), Comparison of Thermospheric Parameters from Space-and Ground-Based Instruments, Ph.D. thesis, Luleå University of Technology.

Killeen, T., F. McCormac, A. Burns, J. Thayer, R. Johnson, and R. Niciejewski (1991), On the dynamics and composition of the high-latitude thermosphere, *J. Atmos. Terr. Phys.*, *53*(9), 797–814, doi:10.1016/0021-9169(91)90095-O.

Killeen, T. L. (1987), Energetics and dynamics of the Earth's thermosphere, *Rev. Geophys.*, *25*(3), 433–454.

Killeen, T. L., and R. G. Roble (1984), An analysis of the high-latitude thermospheric wind pattern calculated by a thermospheric general circulation model: 1. Momentum forcing, *J. Geophys. Res.*, *89*(A9), 7509–7522.

Killeen, T. L., and R. G. Roble (1986), An analysis of the high-latitude thermospheric wind pattern calculated by a thermospheric general circulation model: 2. Neutral parcel transport, *J. Geophys. Res.*, *91*(A10), 11,291, doi:10.1029/JA091iA10p11291.

Killeen, T. L., and R. G. Roble (1988), Thermosphere dynamics: Contributions from the first 5 years of the Dynamics Explorer Program, *Rev. Geophys.*, *26*(2), 329–367, doi:10.1029/RG026i002p00329.

Killeen, T. L., P. B. Hays, N. W. Spencer, and L. E. Wharton (1982), Neutral winds in the polar thermosphere as measured from Dynamics Explorer, *Geophys. Res. Lett.*, *9*(9), 957–960, doi:10.1029/GL009i009p00957.

Killeen, T. L., R. G. Roble, R. W. Smith, N. W. Spencer, J. W. Meriwether, D. Rees, G. Hernandez, P. B. Hays, L. L. Cogger, D. P. Sipler, M. A. Biondi, and C. A. Tepley (1986), Mean neutral circulation in the winter polar F region, *J. Geophys. Res. Sp. Phys.*, *91*(A2), 1633–1649, doi:10.1029/JA091iA02p01633.

Killeen, T. L., J. D. Craven, L. A. Frank, J.-J. Ponthieu, N. W. Spencer, R. A. Heelis, L. H. Brace, R. G. Roble, P. B. Hays, and G. R. Carignan (1988), On the relationship between dynamics of the polar thermosphere and morphology of the aurora: Global-scale observations from Dynamics Explorers 1 and 2, *J. Geophys. Res.*, *93*(A4), 2675, doi:10.1029/JA093iA04p02675.

Killeen, T. L., Y.-I. Won, R. J. Niciejewski, and A. G. Burns (1995), Upper thermosphere winds and temperatures in the geomagnetic polar cap: Solar cycle, geomagnetic activity, and interplanetary magnetic field dependencies, *J. Geophys. Res.*, *100*(A11), 21,327, doi:10.1029/95JA01208.

Kohl, H., and J. W. King (1967), Atmospheric winds between 100 and 700 km and their effects on the ionosphere, *J. Atmos. Terr. Phys.*, *29*(9), 1045–1062, doi:10.1016/0021-9169(67)90139-0.

Kwak, Y. S., and A. D. Richmond (2007), An analysis of the momentum forcing in the high-latitude lower thermosphere, *J. Geophys. Res.*, *112*(A1), A01,306, doi: 10.1029/2006JA011910.

Kwak, Y. S., and A. D. Richmond (2014), Dependence of the high-latitude lower thermospheric wind vertical vorticity and horizontal divergence on the interplanetary magnetic field, *J. Geophys. Res. Sp. Phys.*, *119*(2), 1356–1368, doi:10.1002/2013JA019589.

Laprise, R. (1992), The resolution of global spectral models, *Bull. Am. Meteorol. Soc.*, *73*(9).

Lee, Y.-S., and G. G. Shepherd (2007), Statistical comparison of WINDII auroral green line emission rate with DMSP/SSJ4 electron energy input for high and low solar flux years, *J. Geophys. Res. Sp. Phys.*, *112*(A12), n/a–n/a, doi:10.1029/2007JA012323.

Liou, K., P. T. Newell, and C.-I. Meng (2001), Seasonal effects on auroral particle acceleration and precipitation, *J. Geophys. Res. Sp. Phys.*, *106*(A4), 5531–5542, doi: 10.1029/1999JA000391.

Liu, H., H. Lühr, V. Henize, and W. Köhler (2005), Global distribution of the thermospheric total mass density derived from CHAMP, *J. Geophys. Res.*, *110*(A4), A04,301, doi:10.1029/2004JA010741.

Liu, H., E. Doornbos, and J. Nakashima (2016), Thermospheric wind observed by GOCE: wind jets and seasonal variations, *J. Geophys. Res. Sp. Phys.*, doi: 10.1002/2016JA022938.

Lühr, H., M. Rother, W. Köhler, P. Ritter, and L. Grunwaldt (2004), Thermospheric upwelling in the cusp region: Evidence from CHAMP observations, *Geophys. Res. Lett.*, *31*(6), n/a–n/a, doi:10.1029/2003GL019314.

Makela, J. J., J. W. Meriwether, Y. Huang, and P. J. Sherwood (2011), Simulation and analysis of a multi-order imaging Fabry-Perot interferometer for the study of thermospheric winds and temperatures, *Appl. Opt.*, *50*(22), 4403–4416, doi:10.1364/ao.50.004403.

Makela, J. J., J. W. Meriwether, A. J. Ridley, M. Ciocca, and M. W. Castellez (2012), Large-scale measurements of thermospheric dynamics with a multisite Fabry-Perot interferometer network: Overview of plans and results from midlatitude measurements, *Int. J. Geophys.*, *2012*(3), 872,140, doi:10.1155/2012/872140.

Mayr, H. G., and I. Harris (1978), Some characteristics of electric field momentum coupling with the neutral atmosphere, *J. Geophys. Res. Sp. Phys.*, *83*(A7), 3327–3336, doi:10.1029/JA083iA07p03327.

McCormac, F. G., and R. W. Smith (1984), The influence of the interplanetary magnetic field Y component on ion and neutral motions in the polar thermosphere, *Geophys. Res. Lett.*, *11*(9), 935–938, doi:10.1029/GL011i009p00935.

McCormac, F. G., T. L. Killeen, E. Gombosi, P. B. Hays, and N. W. Spencer (1985), Configuration of the high-latitude thermosphere neutral circulation for IMF By negative and positive, *Geophys. Res. Lett.*, *12*(4), 155–158, doi:10.1029/GL012i004p00155.

McCormac, F. G., T. L. Killeen, J. P. Thayer, G. Hernandez, C. R. Tschan, J.-J. J. Ponthieu, and N. W. Spencer (1987), Circulation of the polar thermosphere during geomagnetically quiet and active times as observed by Dynamics Explorer 2, *J. Geophys. Res. Sp. Phys.*, *92*(A9), 10,133–10,139, doi:10.1029/JA092iA09p10133.

Mccormac, F. G., T. L. Killeen, and J. P. Thayer (1991), The influence of IMF B(y) on the high-latitude thermospheric circulation during northward IMF, *J. Geophys. Res.*, *96*(A1), 115, doi:10.1029/90JA01996.

Meriwether, J. W. (1983), Observations of thermospheric dynamics at high latitudes from ground and space, *Radio Sci.*, *18*(6), 1035–1052, doi:10.1029/RS018i006p01035.

Meriwether, J. W., and P. Shih (1987), On the nighttime signatures of thermospheric winds observed at Sondrestrom, Greenland, as correlated with interplanetary magnetic field parameters, *URSI High Alt. Obs.*, *5*, 329–336.

Meriwether, J. W., J. P. Heppner, J. D. Stolarik, and E. M. Wescott (1973), Neutral winds above 200 km at high latitudes, *J. Geophys. Res.*, *78*(28), 6643–6661, doi:10.1029/JA078i028p06643.

Meriwether, J. W., P. Shih, T. L. Killeen, V. B. Wickwar, and R. G. Roble (1984), Nighttime thermospheric winds over Sondre Stromfjord, Greenland, *Geophys. Res. Lett.*, *11*(9), 931–934, doi:10.1029/GL011i009p00931.

Meriwether, J. W., T. L. Killeen, F. G. McCormac, A. G. Burns, and R. G. Roble (1988), Thermospheric winds in the geomagnetic polar cap for solar minimum conditions, *J. Geophys. Res.*, *93*(A7), 7478, doi:10.1029/JA093iA07p07478.

Mikkelsen, I. S., and M. F. Larsen (1983), An analytic solution for the response of the neutral atmosphere to the high-latitude convection pattern, *J. Geophys. Res.*, *88*(3), 8073–8080, doi:10.1029/JA088iA10p08073.

Morse, P. M., and H. Feshbach (1953), *Methods of Theoretical Physics*, McGraw-Hill, New York.

Niciejewski, R. J., J. W. Meriwether, F. G. McCormac, J. H. Hecht, A. B. Christensen, G. G. Sivjee, D. J. Strickland, G. Swenson, S. B. Mende, A. Vallance Jones, R. L. Gattinger, H. C. Carlson, and C. E. Valladares (1989), Coordinated satellite and ground-based measurements of the energy characteristics of a Sun-aligned arc over Søndre Strømfjord, *J. Geophys. Res.*, *94*(A12), 17,201, doi:10.1029/JA094iA12p17201.

Niciejewski, R. J., T. L. Killeen, R. M. Johnson, and J. P. Thayer (1992), The behavior of the high-latitude F-region neutral thermosphere in relation to IMF parameters, *Adv. Sp. Res.*, *12*(6), 215–218, doi:10.1016/0273-1177(92)90058-6.

Niciejewski, R. J., T. L. Killeen, and S. C. Solomon (1996), Observations of thermospheric horizontal neutral winds at Watson Lake, Yukon Territory (Λ = 65N), *J. Geophys. Res. Sp. Phys.*, *101*(A1), 241–259, doi:10.1029/95JA02683.

Rees, D., and T. J. Fuller-Rowell (1989), Seasonal and geomagnetic response of the thermosphere and ionosphere, *42 AGARD Symp. Ionos. Struct. Var. a Glob. Scale Interact. with Atmos. Magnetos.*

Richmond, A. D. (1995), Ionospheric Electrodynamics Using Magnetic Apex Coordinates., *J. Geomagn. Geoelectr.*, *47*(2), 191–212, doi:10.5636/jgg.47.191.

Richmond, A. D., C. Lathuillere, and S. Vennerstroem (2003), Winds in the high-latitude lower thermosphere: Dependence on the interplanetary magnetic field, *J. Geophys. Res.*, *108*(A2), 1066, doi:10.1029/2002JA009493.

Ridley, A. J. (2007), Effects of seasonal changes in the ionospheric conductances on magnetospheric field-aligned currents, *Geophys. Res. Lett.*, *34*(5), doi: 10.1029/2006GL028444.

Roble, R. G., R. E. Dickinson, and E. C. Ridley (1982), Global circulation and temperature structure of thermosphere with high-latitude plasma convection, *J. Geophys. Res. Sp. Phys.*, *87*(A3), 1599–1614, doi:10.1029/JA087iA03p01599.

Shepherd, G. G., G. Thuillier, W. A. Gault, B. H. Solheim, C. Hersom, J. M. Alunni, J.-F. Brun, S. Brune, P. Charlot, L. L. Cogger, D.-L. Desaulniers, W. F. J. Evans, R. L. Gattinger, F. Girod, D. Harvie, R. H. Hum, D. J. W. Kendall, E. J. Llewellyn, R. P. Lowe, J. Ohrt, F. Pasternak, O. Peillet, I. Powell, Y. Rochon, W. E. Ward, R. H. Wiens, and J. Wimperis (1993), WINDII, the wind imaging interferometer on the Upper Atmosphere Research Satellite, *J. Geophys. Res.*, *98*(D6), 10,725, doi:10.1029/93JD00227.

Shepherd, G. G., G. Thuillier, Y.-M. Cho, M.-L. Duboin, W. F. J. Evans, W. A. Gault, C. Hersom, D. J. W. Kendall, C. Lathuillère, R. P. Lowe, I. C. McDade, Y. J. Rochon, M. G. Shepherd, B. H. Solheim, D.-Y. Wang, and W. E. Ward (2012), The Wind Imaging Interferometer (WINDII) on the Upper Atmosphere Research Satellite: A 20 year perspective, *Rev. Geophys.*, *50*(2), RG2007, doi:10.1029/2012RG000390.

Sica, R. J., M. H. Rees, R. G. Roble, G. Hernandez, and G. J. Romick (1986), The altitude region sampled by ground-based Doppler temperature measurements of the OI 15867 K emission line in aurorae, *Planet. Sp. Sci.*, *34*(5), 483–488, doi: http://dx.doi.org/10.1016/0032-0633(86)90035-8.

Sica, R. J., G. Hernandez, B. A. Emery, R. G. Roble, R. W. Smith, and M. H. Rees (1989), The control of auroral zone dynamics and thermodynamics by the interplanetary magnetic field dawn-dusk (Y) component, *J. Geophys. Res.*, *94*(A9), 11,921, doi:10.1029/JA094iA09p11921.

Sipler, D. P., M. E. Hagan, M. E. Zipf, and M. A. Biondi (1991), Combined optical and radar wind measurements in the F region over Millstone Hill, *J. Geophys. Res.*, *96*(A12), 21,255, doi:10.1029/91JA02371.

Sojka, J. J., R. W. Schunk, and W. J. Raitt (1982), Seasonal variations of the high-latitude F region for strong convection, *J. Geophys. Res.*, *87*(A1), 187, doi: 10.1029/JA087iA01p00187.

Spencer, N. W., L. E. Wharton, H. B. Niemann, A. E. Hedin, G. R. Carrignan, and J. C. Maurer (1981), The Dynamics Explorer Wind and Temperature Spectrometer, *Sp. Sci. Instrum.*, *5*, 417–428.

Spencer, N. W., L. E. Wharton, G. R. Carignan, and J. C. Maurer (1982), Thermosphere zonal winds, vertical motions and temperature as measured from Dynamics Explorer, *Geophys. Res. Lett.*, *9*(9), 953–956, doi:10.1029/GL009i009p00953.

Swarztrauber, P. N. (1993), The Vector Harmonic Transform Method for Solving Partial Differential Equations in Spherical Geometry, *Mon. Weather Rev.*, *121*(12), 3415–3437, doi:10.1175/1520-0493(1993)121¡3415:TVHTMF¿2.0.CO;2.

Thayer, J. P., and T. L. Killeen (1991), Vorticity and divergence in the high-latitude upper thermosphere, *Geophys. Res. Lett.*, *18*(4), 701–704, doi:10.1029/91GL00131.

Thayer, J. P., and T. L. Killeen (1993), A kinematic analysis of the high-latitude thermospheric neutral circulation pattern, *J. Geophys. Res.*, *98*(93), 11,549–11,565, doi: 10.1029/93JA00629.

Volland, H. (1979), Magnetospheric electric fields and currents and their influence on large scale thermospheric circulation and composition, *J. Atmos. Terr. Phys.*, *41*(7-8), 853–866, doi:10.1016/0021-9169(79)90128-4.

Wharton, L. E., N. W. Spencer, and H. G. Mayr (1984), The Earth's thermospheric superrotation from Dynamics Explorer 2, *Geophys. Res. Lett.*, *11*(5), 531–533, doi: 10.1029/GL011i005p00531.

Witasse, O., J. Lilensten, C. Lathuillere, and B. Pibaret (1998), Meridional thermospheric neutral wind at high latitude over a full solar cycle, *Ann. Geophys.*, *16*(10), 1400–1409, doi:10.1007/s00585-998-1400-3.

Wu, Q., R. D. Gablehouse, S. C. Solomon, T. L. Killeen, and C.-Y. She (2004), A New Fabry-Perot Interferometer for Upper Atmosphere Research, in *Proc. SPIE*, vol. 5660, edited by C. A. Nardell, P. G. Lucey, J.-H. Yee, and J. B. Garvin, pp. 218–227, doi: 10.1117/12.573084.

Wu, Q., D. McEwen, W. Guo, R. Niciejewski, R. Roble, and Y.-I. Won (2008), Long-term thermospheric neutral wind observations over the northern polar cap, *J. Atmos. Solar-Terrestrial Phys.*, *70*(16), 2014–2030, doi:10.1016/j.jastp.2008.09.004.

Xiong, C., H. Lühr, and B. G. Fejer (2015), Global features of the disturbance winds during storm time deduced from CHAMP observations, *J. Geophys. Res. Sp. Phys.*, *120*(6), doi:10.1002/2015JA021302.

Figure 2. Average quiet-time magnetic zonal winds computed from ground-based FPIs (MH=Millstone Hill, SS=Sondrestom, RB=Resolute Bay, TH=Thule), SDIs (PF=Poker Flat, TL=Toolik Lake), WINDII, and DE2 WATS data as a function of season and magnetic local time (MLT, hourly), for successive 5 degree magnetic latitude (MLAT) bins. The blue curve shows average model winds from climatological data assimilation at the locations of observations. The black curve shows model winds at the middle of each magnetic latitude bin. Observed and model winds are hourly averaged. Each column and row represents seasonally and latitudinally binned average winds, respectively. Error bars denote the estimated 1σ uncertainty of the mean. The estimated uncertainty of the mean for each bin was calculated by dividing standard deviation by the square root of the number of days in the sample [Emmert et al., 2002, 2006a]. The wind components are in magnetic directions, except for WATS zonal winds, which are longitudinally averaged geographic zonal winds. Data from various stations are labeled in colors and symbols (presented at the top of the figure).

Figure_2.pdf

Figure 3. Same as Figure 2, but in this case showing meridional winds.

Figure 4. Average quiet-time geographic northward (top) and eastward (bottom) winds from Millstone Hill (MH), Peach Mountain (PM), and Urbana (UR) FPIs compared with modeled wind for December solstice (left), equinox (middle), and June solstice (right). The northward wind data are sorted into measurements north and south of the observing station. The average magnetic latitude of the observations are annotated on the right. Error bars indicate the estimated 1σ uncertainty of the mean. Data from various stations are labeled in colors and symbols shown at the top of the figure.

Figure 5. Average quiet-time magnetic zonal winds computed from FPIs, SDIs, WINDII, and DE2 WATS data as a function of season and magnetic latitude (MLAT, 2 degree bin), for successive 2 hour magnetic local time (MLT) bins. The blue curve shows average model winds from climatological data assimilation at the locations of observations. The black curve shows model winds at the middle of each local time bin. Each column and row represents seasonally and local time binned averaged winds, respectively. Error bars denote the estimated uncertainty of the mean (spread of 1σ around the mean) . The wind components are in magnetic directions, except for WATS zonal winds, which are longitudinally averaged geographic zonal winds. Data from various stations are labeled in colors and symbols (presented at the top of the figure).

Figure 6. Same as Figure 5, but in this case showing meridional winds.

Figure_3.pdf

Figure 7. Average quiet-time cross-track wind observed by GOCE and computed from FPIs, SDIs, and WINDII data as a function of season and magnetic latitude (MLAT, 2 degree bin), for successive 1 hour magnetic local time (MLT) bins around the dusk and dawn time sectors. Black circular symbols show modeled average cross-track wind along the GOCE orbit. The rightmost column shows the direction of the average GOCE cross-track unit vector as function of magnetic latitude. Magnetic north (east) is at the top (right) of the page.

Figure_5.pdf

Figure 8. Average quiet-time cross-track wind observed by GOCE and computed from FPIs, SDIs, and WINDII data as a function of season and magnetic local time (MLT, hourly), for successive 5 degree magnetic latitude (MLAT) bins above 60N MLAT. Black circular symbols show modeled average cross-track wind along the GOCE orbit. The rightmost column shows the direction of the GOCE cross-track unit vector as a function of MLT. Magnetic north (east) is at the top (right) of the page.

Figure_7.pdf

Figure_6.pdf

Figure 9. Quiet-time average F-region assimilated neutral vector winds as a function of magnetic latitude and local time at northern high latitudes (looking down on the geomagnetic north pole). Results are shown for December solstice, equinox, and June solstice. The background color represents the magnitude of wind speed. The same wind vector scaling (vector scale shown on the top) was used for each vector wind field.

Figure 10. Interseasonal comparison of quiet-time modeled average neutral zonal (left) and meridional (right) winds as a function of magnetic local solar time at various northern high latitudes (annotated on the right).

Figure 11. Quiet-time variation in assimilated zonal (top row) and meridional wind fields (bottom row), as a function of magnetic local time and magnetic latitude. Results are shown for December solstice, equinox, and June solstice. Wind contours are separated by 30 ms^{-1}.

Figure 12. Vorticity of the empirically modeled quiet-time high latitude vector wind fields as a function of magnetic latitude and magnetic local solar time.

Figure 13. Same as Figure 12, but in this case showing divergence fields.

Table 1. Quiet time observational wind data sets used. Data only above 45N magnetic latitude are shown.

Station	Magnetic Latitude	Years of Data	Height (km)	Local Time	Days	Data Points	<$F_{10.7}$ (sfu)>	References
Fabry-Perot Interferometers (ground-based)								
Thule	84.6N	1987	250	night	57	4949	99.50	Killeen et al. [1995]
Resolute Bay	83.4N	2004-2007	250	night	216	8176	98.70	Wu et al. [2004]
Søndre Strømfjord	73.3N	1983-1984, 1987-1995, 2002-2004	250	night	566	26708	109.3	Killeen et al. [1995]
Millstone Hill	53.1N	1990-2002	250	night	533	13267	116.3	Sipler et al. [1991]
Peach Mountain	52.1N	2012-2015	250	night	507	32968	120.2	Makela et al. [2011]
Urbana	52.1N	2007-2008, 2012-2015	250	night	648	53621	119.5	Makela et al. [2011]
Scanning Doppler Imaging Fabry-Perot Interferometers (ground-based)								
Toolik Lake	68.3N	2012-2014	250	night	198	123801	120.3	Conde and Smith [1995
Poker Flat	65.2N	2010-2012	250	night	303	114933	114.9	Conde and Smith [1995
Space-based Instruments								
DE2 WATS	89.5N-89.8S	1981-1983	210-320	both	55	4781	135.6	Spencer et al. [1981]
WINDII 557.7 nm	81.6N-88.0S	1991-1997	210-320	day	198	16582	112.2	Shepherd et al. [1993]
WINDII 630.0 nm	80.1N-86.0S	1991-1997	210-320	night	77	3402	103.0	Shepherd et al. [1993]
GOCE	90.0N-89.8S	2009-2012	253-295	twilight	571	51203	104.3	Doornbos et al. [2014]

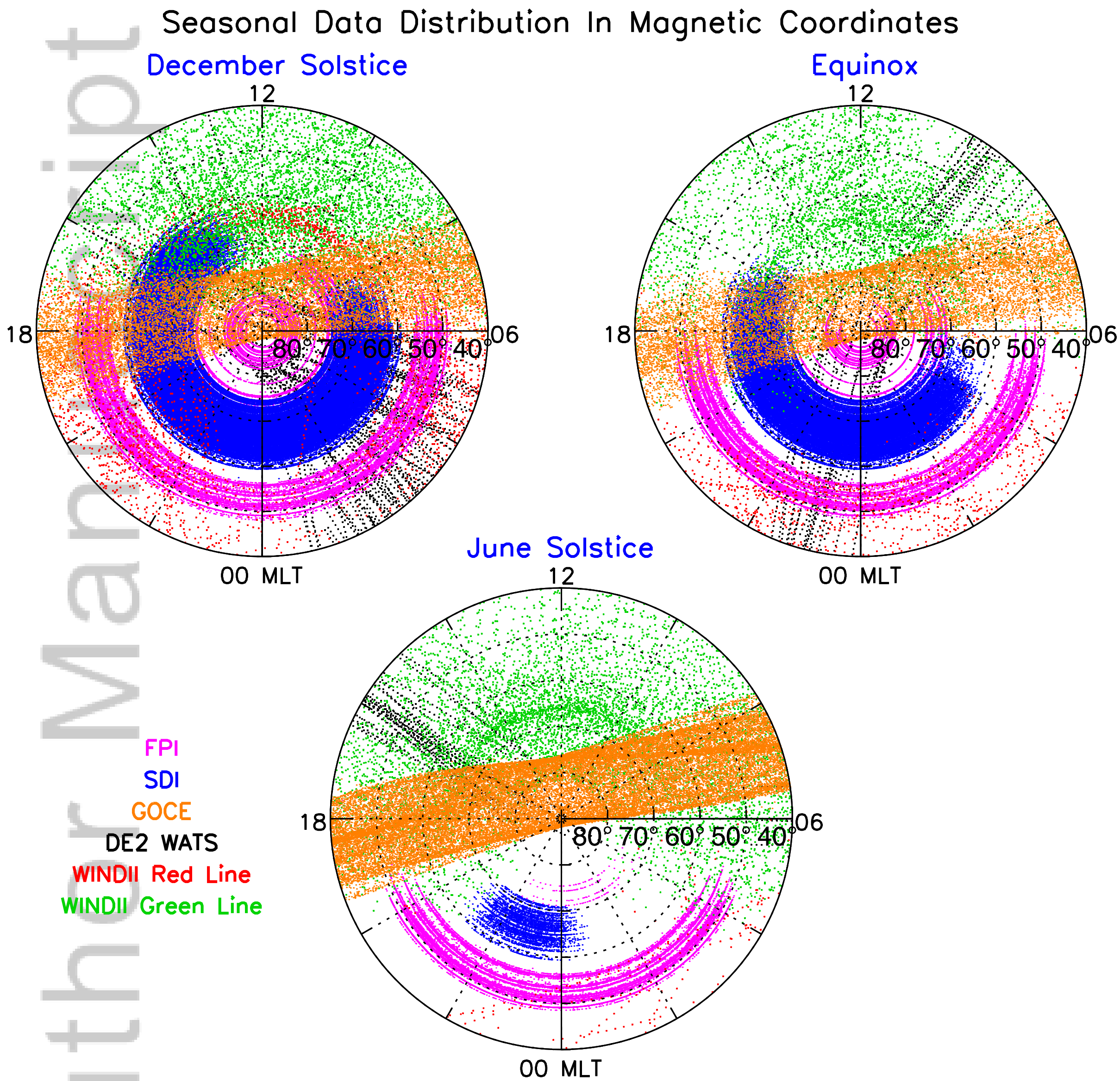

Seasonal Data Distribution In Magnetic Coordinates
December Solstice
Equinox
June Solstice
12
18
06
00 MLT
80° 70° 60° 50° 40°
FPI
SDI
GOCE
DE2 WATS
WINDII Red Line
WINDII Green Line

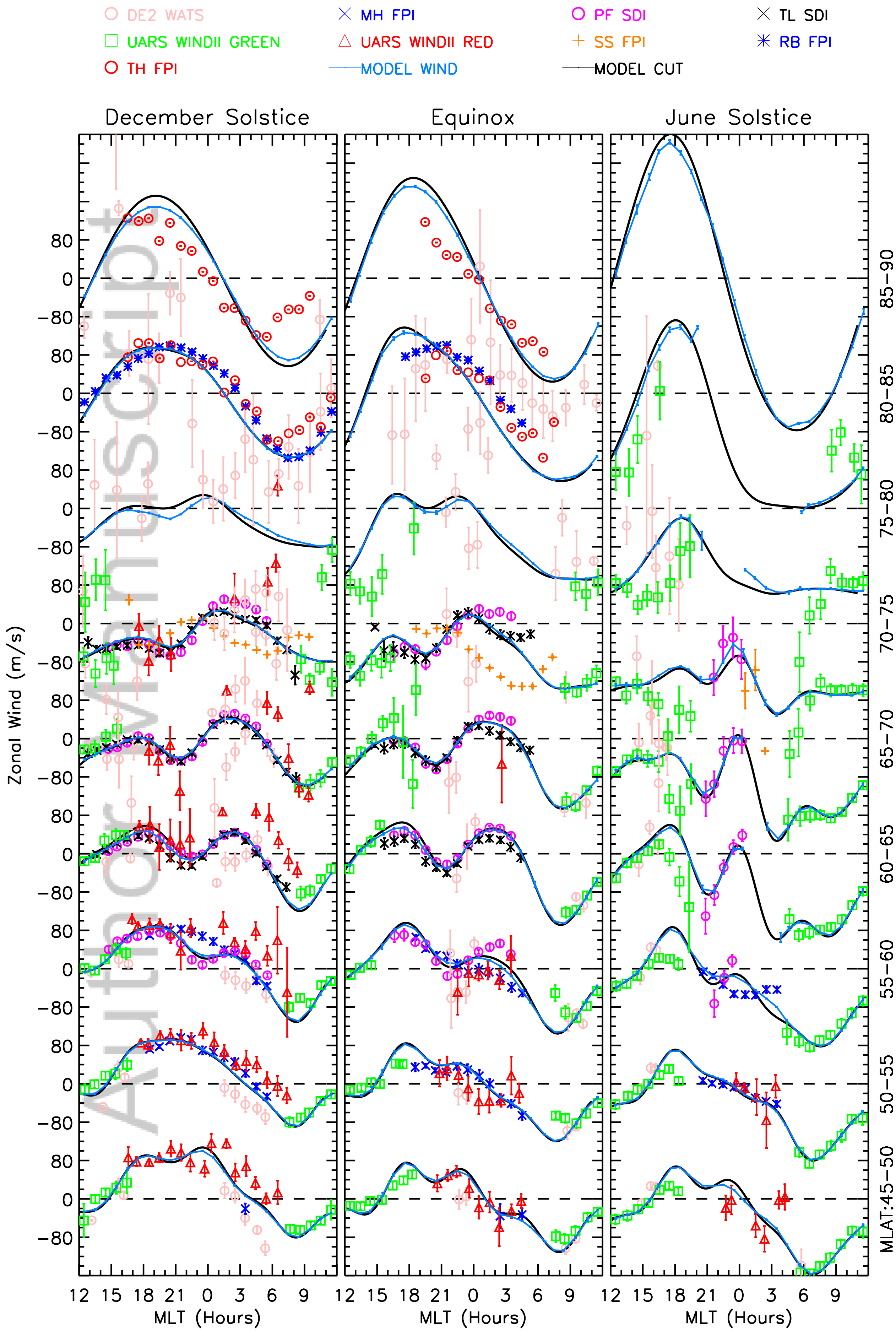

DE2 WATS
UARS WINDII GREEN
TH FPI
MH FPI
UARS WINDII RED
MODEL WIND
PF SDI
SS FPI
MODEL CUT
TL SDI
RB FPI
December Solstice
Equinox
June Solstice
Zonal Wind (m/s)
MLT (Hours)
85–90
80–85
75–80
70–75
65–70
60–65
55–60
50–55
MLAT:45–50

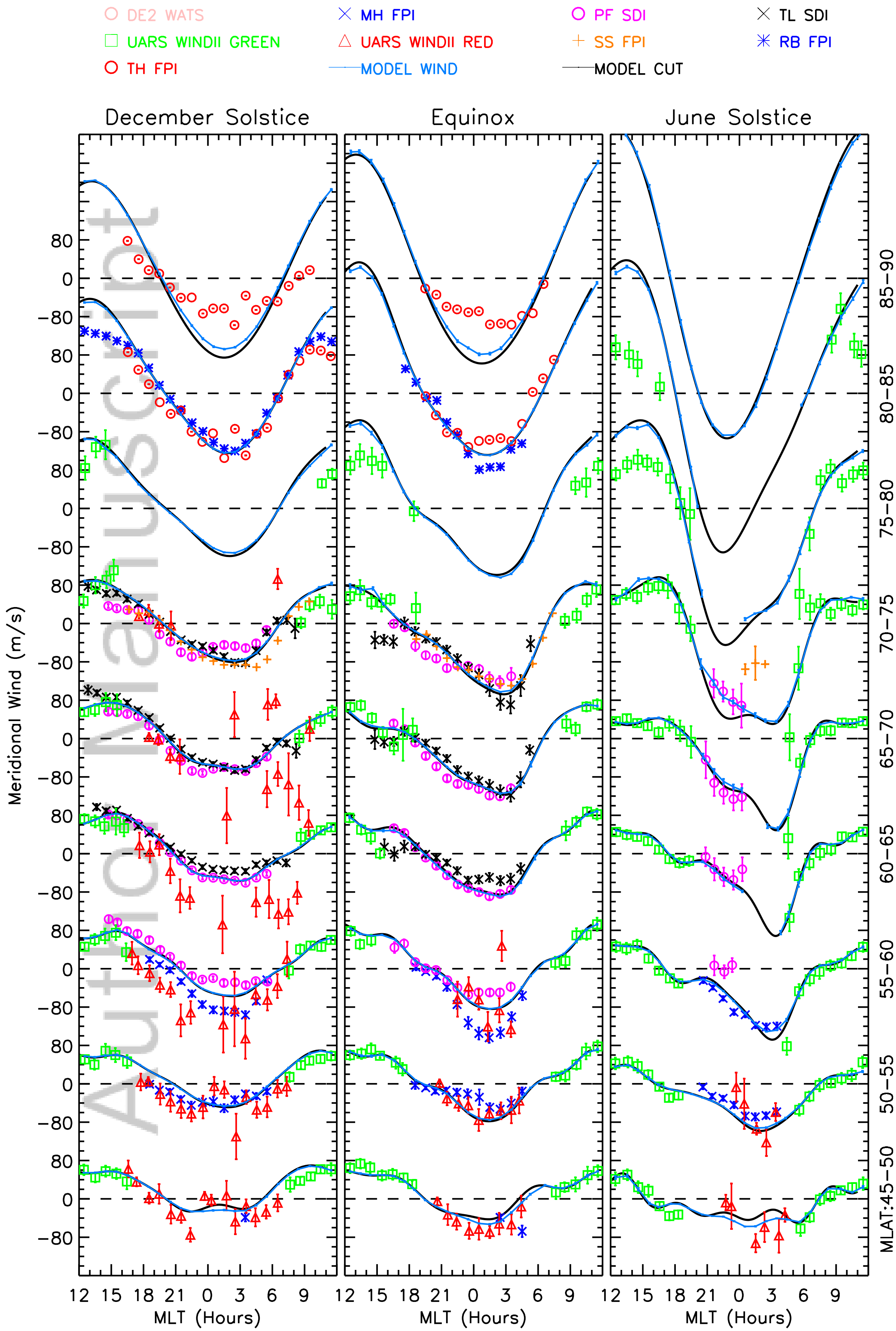

DE2 WATS
MH FPI
PF SDI
TL SDI
UARS WINDII GREEN
UARS WINDII RED
SS FPI
RB FPI
TH FPI
MODEL WIND
MODEL CUT
December Solstice
Equinox
June Solstice
Meridional Wind (m/s)
MLT (Hours)
85–90
80–85
75–80
70–75
65–70
60–65
55–60
50–55
MLAT:45–50

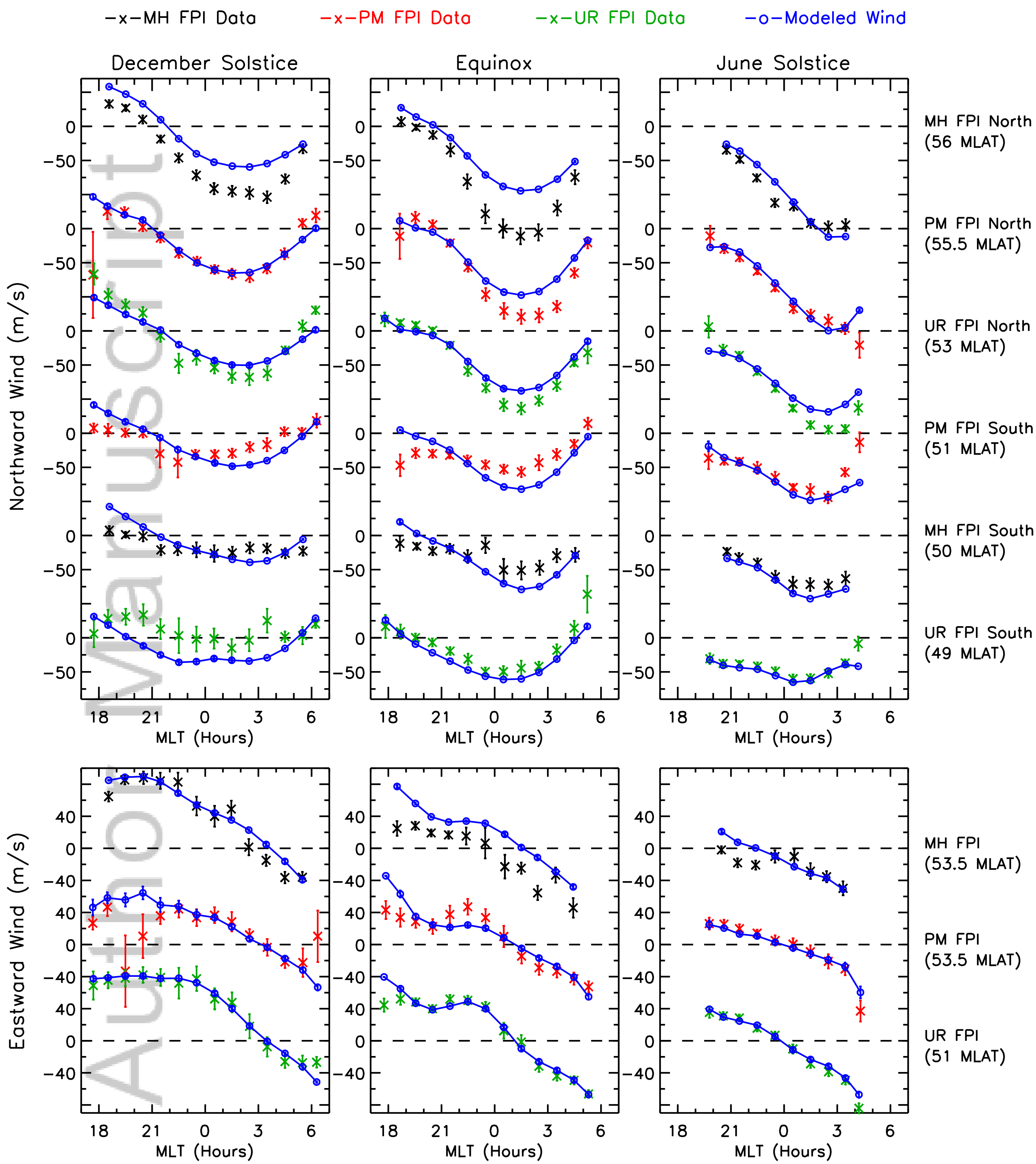

−x−MH FPI Data
−x−PM FPI Data
−x−UR FPI Data
−o−Modeled Wind
December Solstice
Equinox
June Solstice
Northward Wind (m/s)
Eastward Wind (m/s)
MLT (Hours)
MH FPI North
(56 MLAT)
PM FPI North
(55.5 MLAT)
UR FPI North
(53 MLAT)
PM FPI South
(51 MLAT)
MH FPI South
(50 MLAT)
UR FPI South
(49 MLAT)
MH FPI
(53.5 MLAT)
PM FPI
(53.5 MLAT)
UR FPI
(51 MLAT)

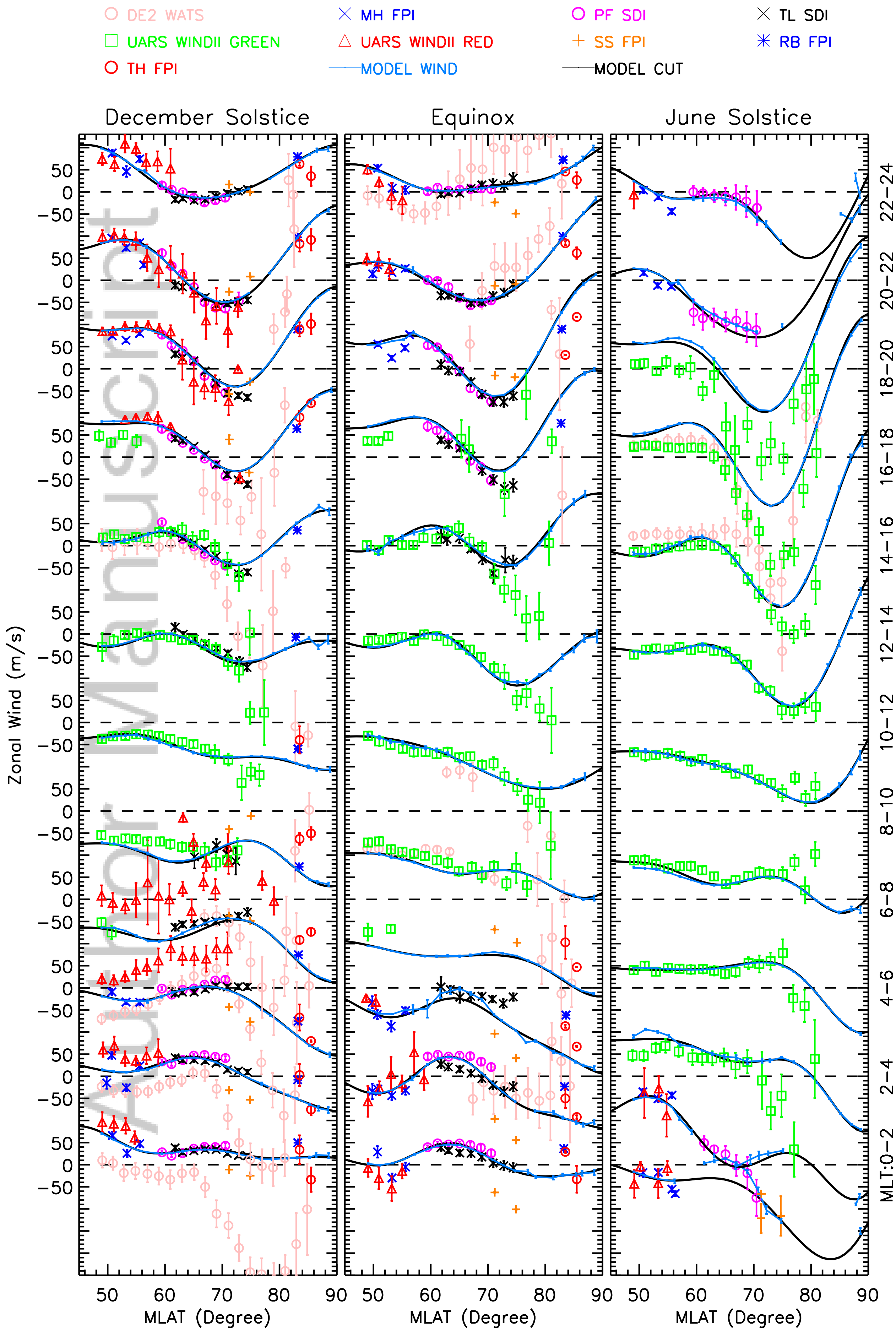
DE2 WATS
UARS WINDII GREEN
TH FPI
MH FPI
UARS WINDII RED
MODEL WIND
PF SDI
SS FPI
MODEL CUT
TL SDI
RB FPI
December Solstice
Equinox
June Solstice
Zonal Wind (m/s)
MLAT (Degree)
MLT:0−2
2−4
4−6
6−8
8−10
10−12
12−14
14−16
16−18
18−20
20−22
22−24

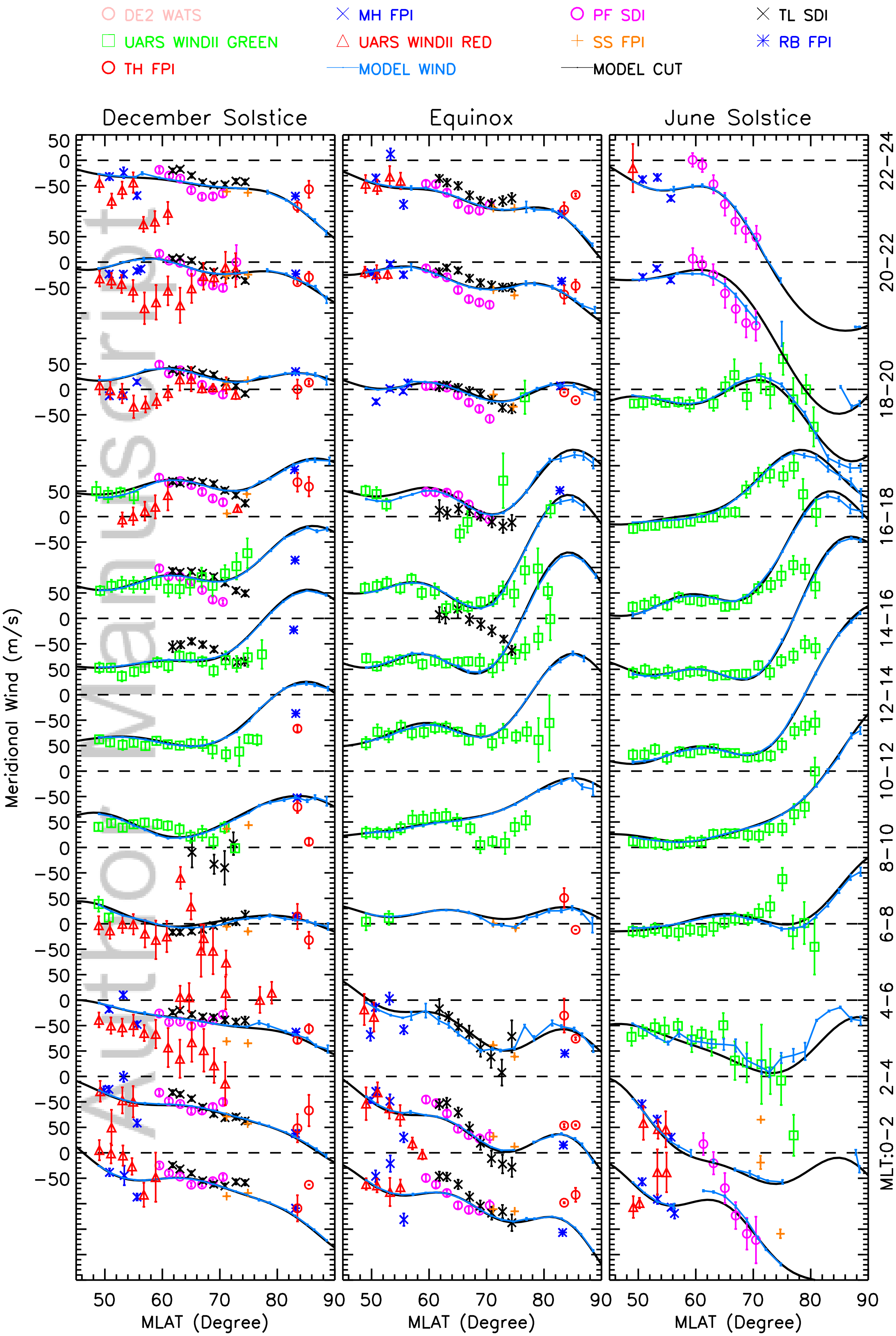
DE2 WATS
MH FPI
PF SDI
TL SDI
UARS WINDII GREEN
UARS WINDII RED
SS FPI
RB FPI
TH FPI
MODEL WIND
MODEL CUT
December Solstice
Equinox
June Solstice
Meridional Wind (m/s)
MLAT (Degree)
22−24
20−22
18−20
16−18
14−16
12−14
10−12
8−10
6−8
4−6
2−4
MLT:0−2

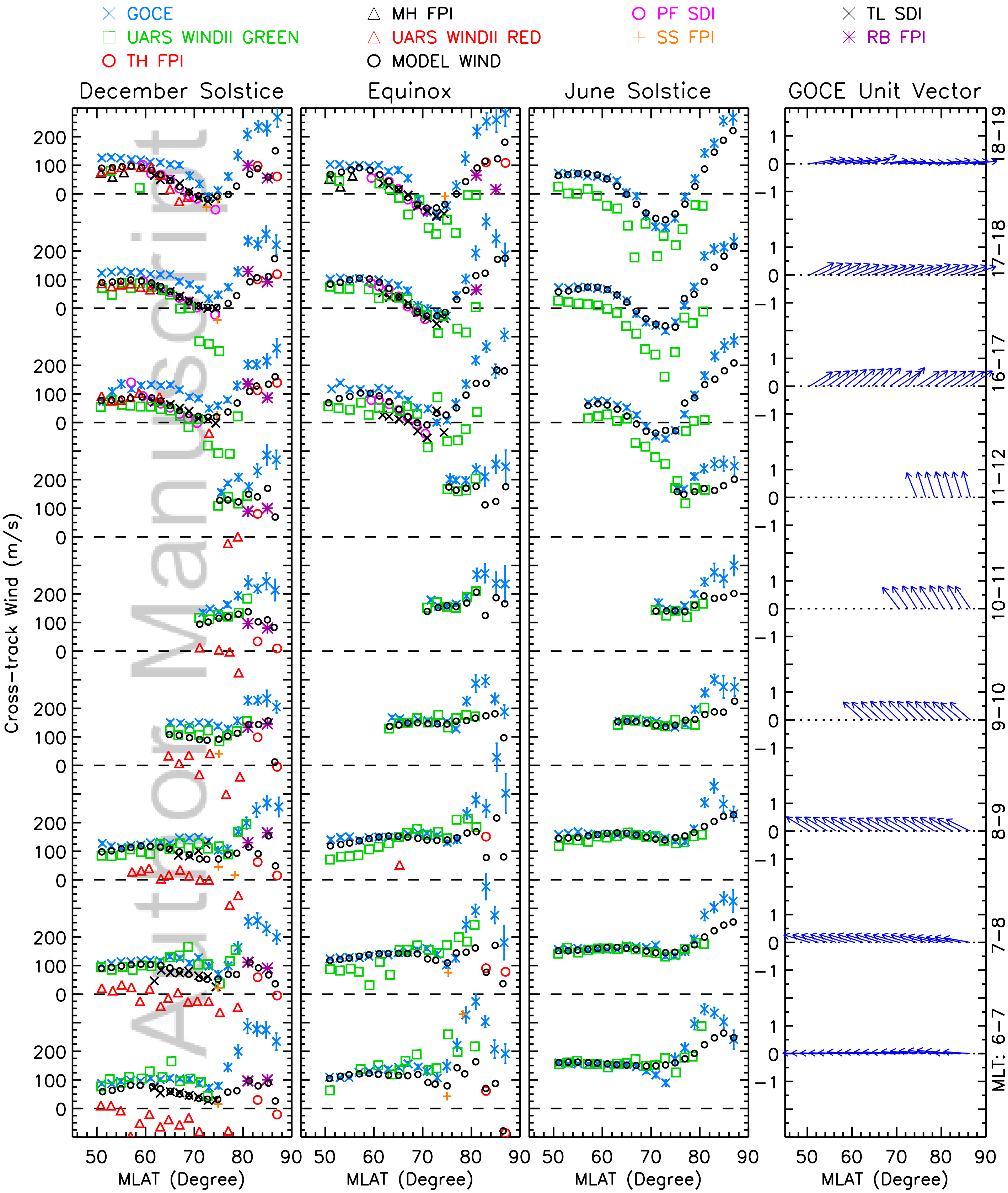

GOCE
UARS WINDII GREEN
TH FPI
MH FPI
UARS WINDII RED
MODEL WIND
PF SDI
SS FPI
TL SDI
RB FPI
December Solstice
Equinox
June Solstice
GOCE Unit Vector
Cross-track Wind (m/s)
MLAT (Degree)
MLT: 6–7
7–8
8–9
9–10
10–11
11–12
16–17
17–18
18–19

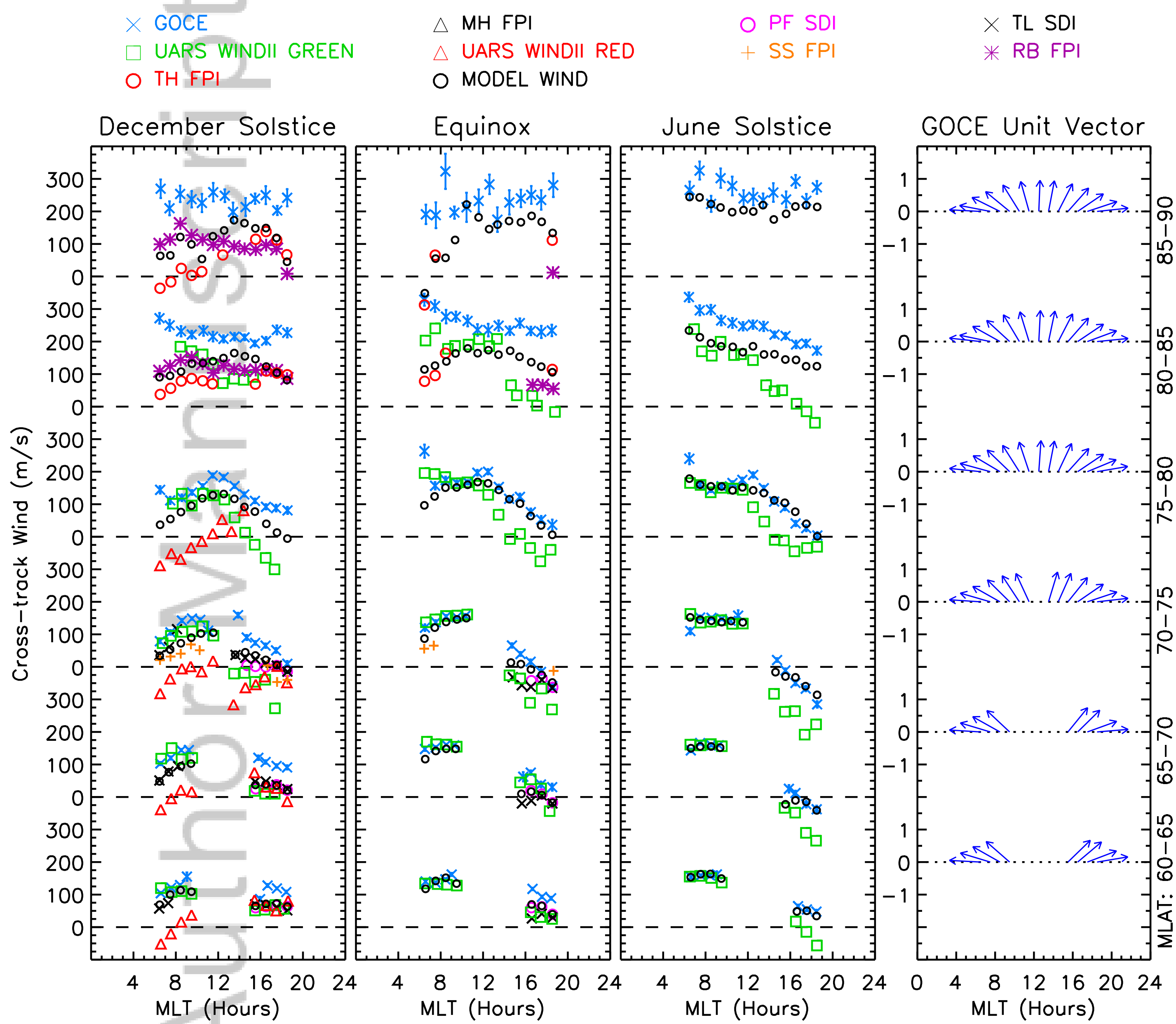
GOCE
UARS WINDII GREEN
TH FPI
MH FPI
UARS WINDII RED
MODEL WIND
PF SDI
SS FPI
TL SDI
RB FPI
December Solstice
Equinox
June Solstice
GOCE Unit Vector
Cross-track Wind (m/s)
MLT (Hours)
MLT (Hours)
MLT (Hours)
MLT (Hours)
85-90
80-85
75-80
70-75
65-70
MLAT: 60-65

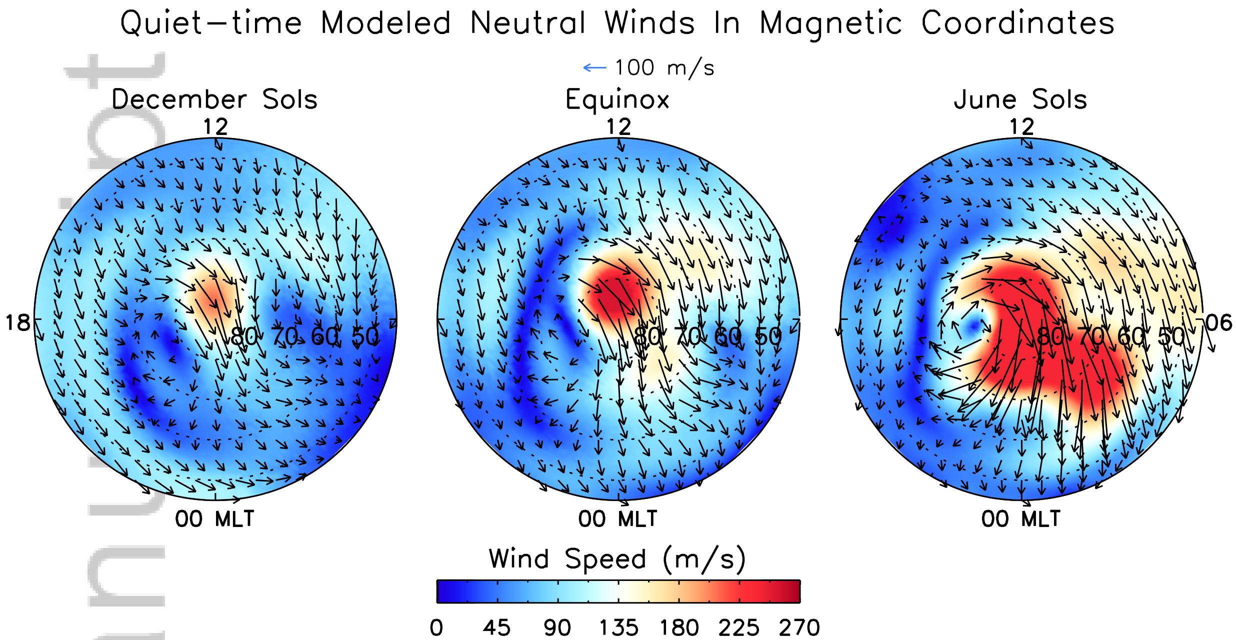
Quiet−time Modeled Neutral Winds In Magnetic Coordinates
100 m/s
December Sols
Equinox
June Sols
12
18
06
80 70 60 50
00 MLT
Wind Speed (m/s)
0 45 90 135 180 225 270

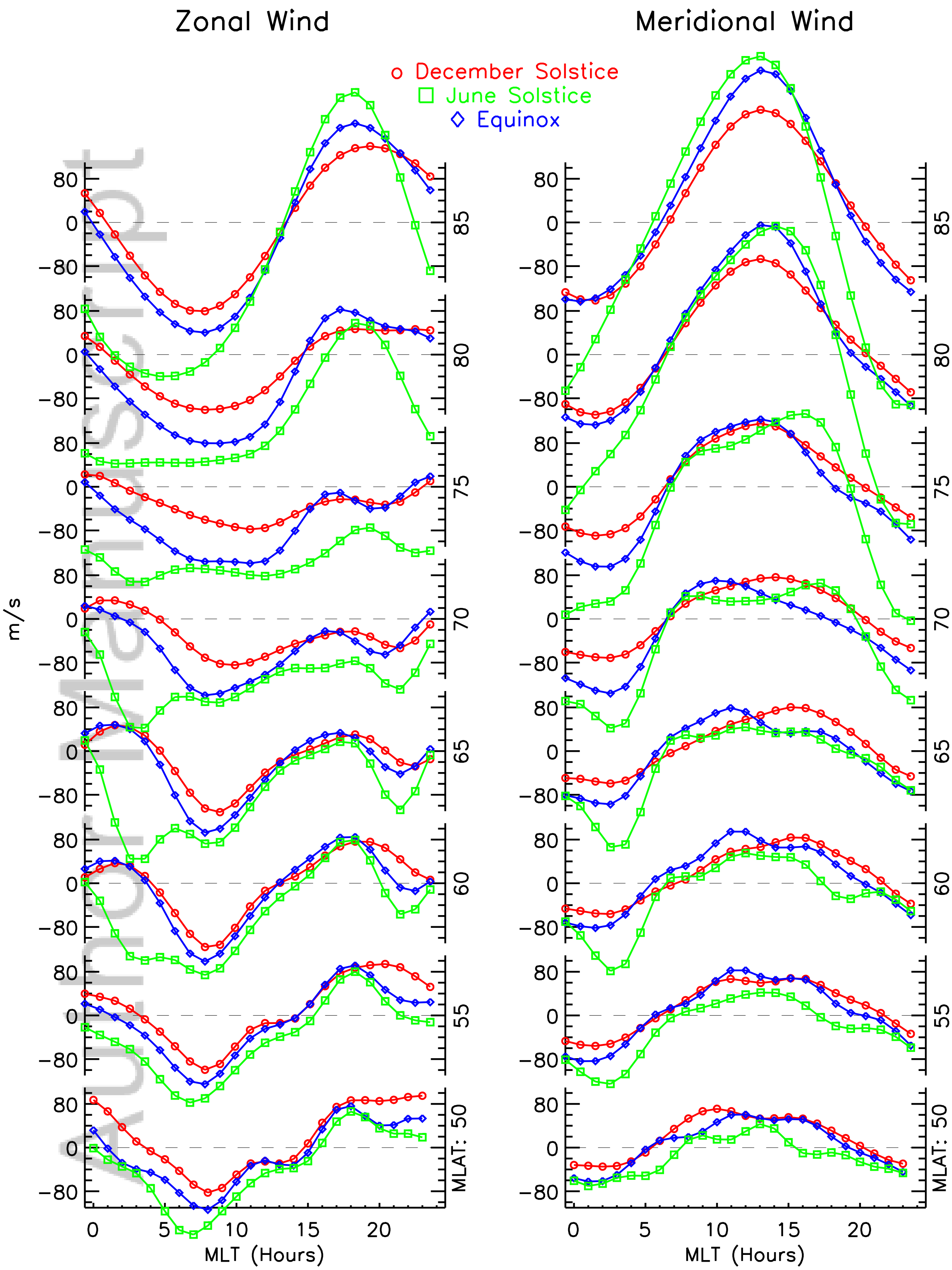
Zonal Wind
Meridional Wind
o December Solstice
□ June Solstice
◇ Equinox
m/s
80
0
−80
85
80
75
70
65
60
55
MLAT: 50
0
5
10
15
20
MLT (Hours)
Author Manuscript

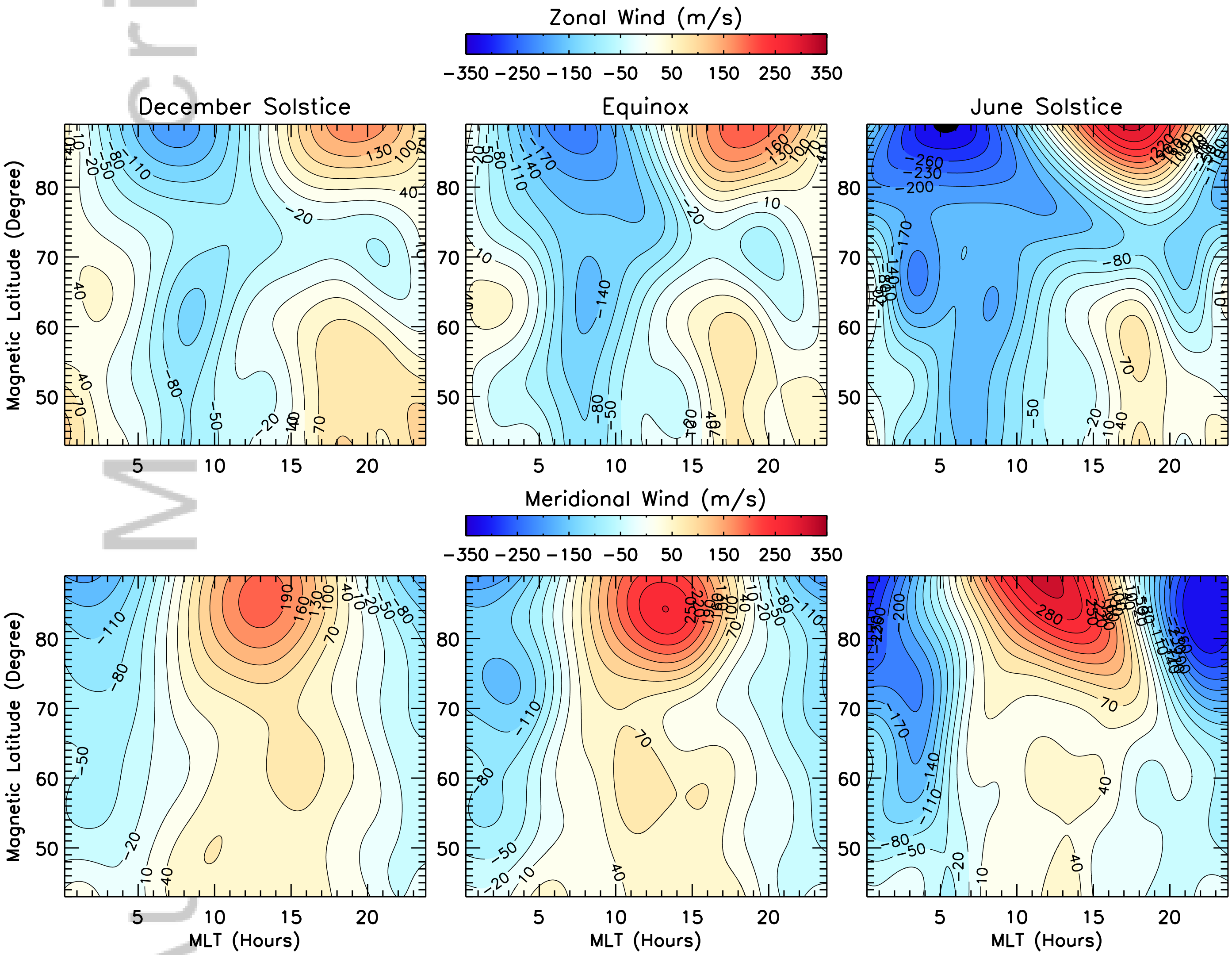
Zonal Wind (m/s)
−350 −250 −150 −50 50 150 250 350
December Solstice
Equinox
June Solstice
Magnetic Latitude (Degree)
Meridional Wind (m/s)
−350 −250 −150 −50 50 150 250 350
MLT (Hours)

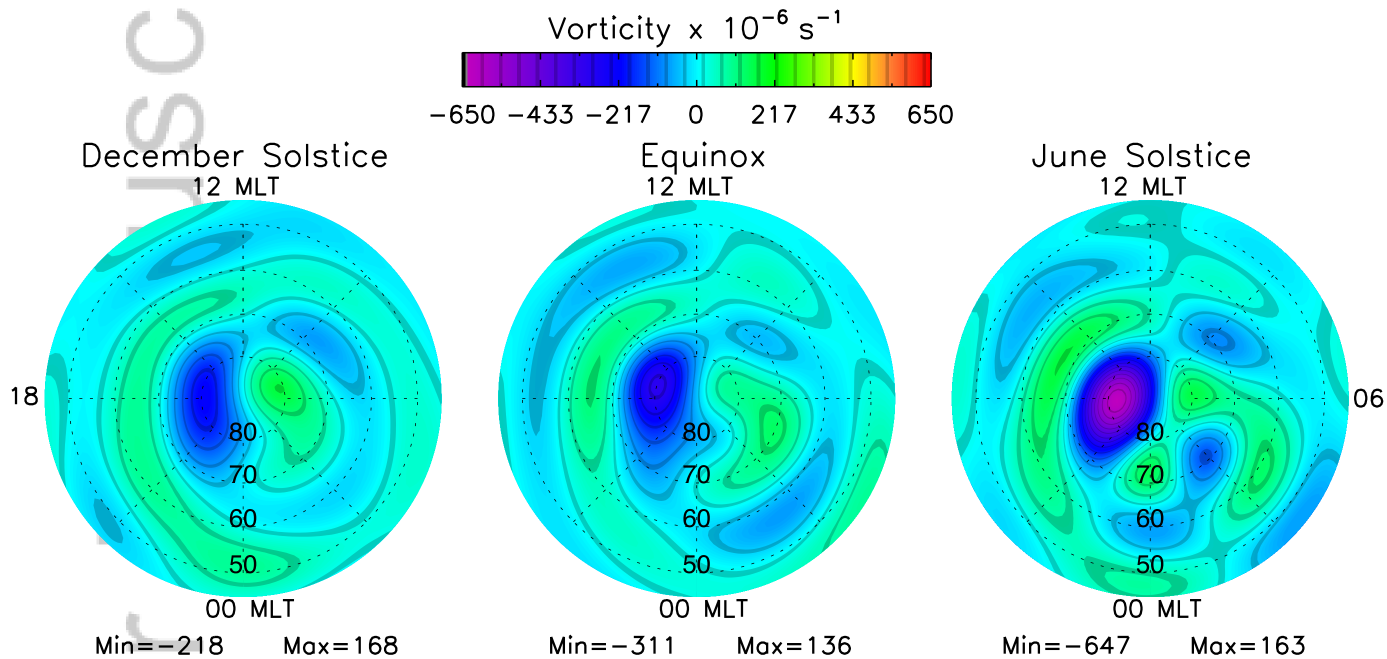

Vorticity x 10^{-6} s^{-1}
−650 −433 −217 0 217 433 650
December Solstice
Equinox
June Solstice
12 MLT
18
06
80
70
60
50
00 MLT
Min=−218 Max=168
Min=−311 Max=136
Min=−647 Max=163

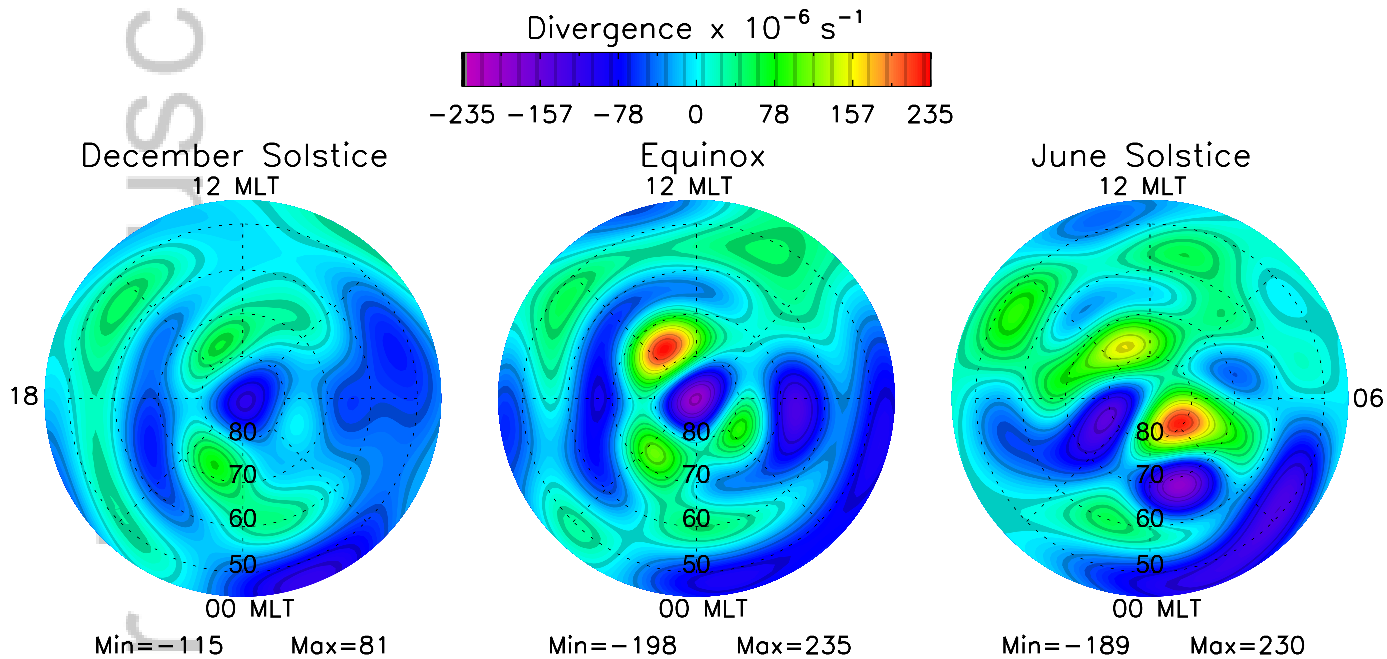
Divergence x 10^{-6} s^{-1}
−235 −157 −78 0 78 157 235
December Solstice
Equinox
June Solstice
12 MLT
18
06
80
70
60
50
00 MLT
Min=−115 Max=81
Min=−198 Max=235
Min=−189 Max=230